A critical comparison of shear tests for adhesive joints

Alexandre Jouan, Andrei Constantinescu

a critical comparison of shear tests for adhesive joints

Alexandre Jouan*, Andrei Constantinescu

Laboratoire de Mécanique des Solides, CNRS, Ecole Polytechnique, Université Paris-Saclay, 91120 Palaiseau, France, alexandre.jouan@polytechnique.edu, andrei.constantinescu@polytechnique.edu

*Corresponding author

Abstract:

Adhesive joints get a growing part of assembly solutions in various industrial applications and are considered as an alternative to soldering and welding. Their small thickness to length or aspect ratio and the importance of the interface with the assembled parts increase the difficulties for measuring their characteristic mechanical properties such as constitutive law, endurance limit, etc… Several testing configurations and methods have been proposed in the literature without a clear emergence of an optimal configuration. This paper proposes a critical review of four different methods taken from the literature and industrial standards: the single lap joint shear test, the thick adherent shear test, the ARCAN test and napkin ring test. In order to contribute to the emergence and to help the experimentalist find an optimal specimen design, the heterogeneities of stress and strain field distributions are here discussed. The test specimens and configurations under scrutiny are compared using both closed-form expressions and Finite-Element computations and considering two different criteria: the spatial distribution of shear stress and the triaxiality ratio between normal and shear stresses in the joint. This study highlights both advantages and limits of each method for mechanical behavior and fatigue characterization. As a final consequence of the remarks an optimal specimen configuration is proposed.

Keywords: adhesive joint; experimental setup; stress homogeneity; triaxiality ratio

1. Introduction

In the last decades, adhesive joints (also denoted as “adhesive layer”) obtained a growing share of the bonding and assembly solutions in various industries. This is illustrated by technical studies across various fields like aeronautics and automotive , seawater , offshore and electronics. The replacement of soldering and welding by adhesive bonding has brought several advantages up: an easier assembly process, lower temperatures during the manufacturing process, an alternative to lead soldering, the possibility to bind diverse materials together. The extending area of utilization requires novel mechanical tests to assess the behavior and the reliability of the joints.

Adhesive joints are not always homogeneous materials, but rather often complex composite materials with specific microstructures. They usually consist of a polymer matrix and filler particles. The fillers improve the mechanical properties and can also add electrical or thermal properties to the behavior of the adhesive joint. The dimensions of the adhesive joint are characterized by a small thickness when compared with the two in-plane directions. This geometric feature adds further difficulties when measuring the properties or proposing models to characterize their behavior. Moreover, the small thickness will increase the importance of the interfaces in the global behavior of the assembly and the need to characterize it. Technically, these two properties often lead to microscopic homogenization studies and macroscopic model reduction.

Therefore, there is a specific need to design specific test geometries other than a classical tensile test specimen (dog bone specimen for example) to access material and interfaces properties of interest. So far, several characterization methods have been proposed and documented in the literature. A first method named the butt joint has a considerable success in the joint community, as it enables a simple manufacturing process and the possibility to perform both tensile and shear tests. One of the key points of this method is the alignment of the substrates, also denoted as adherents, in order to assure a constant thickness during the curing of the joint and a parallel loading during the test. Moreover, in the case of torsional load of the butt joint, the spatial stress and strain distributions within the joint are heterogeneous. Therefore, supplementary numerical corrections are needed for the interpretation of the test results and for acquiring the real material data, as for example the Nadai correction discussed in . Furthermore, in the case of a rate-dependent (viscoelastic) behavior characterization, the strain gradient inside the joint implies a non-uniform strain rate, resulting in a more complex identification procedure. Hence, this method will not be discussed in detail in this paper. Within the methods providing an uniform shear test, one can cite the following groups in order of increasing complexity: the single lap shear test (SLJ), the Thick Adherent Shear Test (TAST) , the ARCAN device , and the napkin ring test . The later measures substantially different parameter values for the same material as observed in , , and . A first comparison of the four method is presented in and is focused on the shear and peel stress state at midplane of the joint. Nevertheless, from the more general point of view of continuum mechanics, it is interesting to focus on the triaxiality ratio which can be related to nonlinear models including viscosity, plasticity or damage . An analysis of the literature reveals that we are still missing simple estimations to distinguish the evolution of the main mechanical variables in the different tests.

This paper proposes to fill this gap by advancing a critical review of the different setups, based upon a precise computation of the stress and strain fields using closed-form expression and numerical techniques. The qualitative and quantitative understanding of the peculiarities of the different methods will finally conduct to the design of an optimal specimen, which will be presented.

The article is organized as follows: it first describes the geometry of the studied test methods. It then introduces notations, assumptions and criteria of comparison, and describes the analytical and numerical method used. Finally, the results are presented and discussed with a focus on the mechanical state at joint mid-plane and joint-substrate interface. As a final consequence of the discussion, a “hybrid” specimen geometry for the test is proposed.

2. Presentation of the test methods

The testing methods exposed next are based on different geometries of the specimen and mechanical setups to transmit the applied loading to the joint. The choice of the adhesive joint thickness h and length L are usually let to the experimentalist. The existing standards rather classically define the dimensions and angles of the substrate and will be presented next. In this paper, all dimensions are given in millimeters by default.

The single lap shear test (SLJ), Thick Adherent Shear Test (TAST), and the ARCAN device are loaded using classical a tensile test machine, whereas the napkin ring test is loaded by a torsional test machine.

2.1. Single lap shear test (SLJ)

In spite of recent developments and criticisms, the lap shear is still the most used method to characterize joint behavior and strength because of its design simplicity. It consists of two rectangular plates (substrates) bonded together by the adhesive joint, as illustrated on Figure 1. The dimensions of the joint are controlled (i.e. length L and thickness h). As already mentioned in the introduction for the butt joint method, the alignment of the substrates and the control of the thickness are two key points to take into account with this geometry. Moreover, special tooling is generally needed to guarantee the rectangular shape of the joint with no overfill or lack of matter at its free edges. The common standards describing this method are ASTM D1002 and ISO 9664. However, the setup does not have the natural symmetries with respect to the adhesive joint and induces as such an additional moment to the loading. This moment causes the substrates to bend, as will be further highlighted.

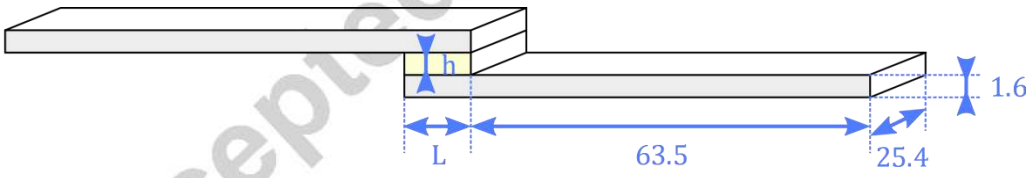

Figure 1: Single lap joint geometry. Dimensions are given in millimeters.

2.2. Thick Adherent Shear Test (TAST)

To overcome the weaknesses of the lap shear geometry, the TAST method was designed with thicker substrates. This change in substrate dimensions (length and thickness) aims at limiting the bending phenomenon of the substrates due to the rotational moment of the assembly during loading. One machined slot per substrate, separated by a distance L (see Figure 2), allows the only overlap of the joint to be solicited during loading. The engineering standards for this geometry are ASTM D3165, ASTM D5656-95 and ISO 11003-2. The ASTM standards set the joint length L to $9.54\ mm$, which is of the same order of magnitude as the substrate thickness. As a consequence, substrates can be considered as thick. Nonetheless, here, L will vary between $10\ mm$ and $30\ mm$ and this variation will permit to highlight its influence on the shear stress homogeneity and on the triaxiality ratio.

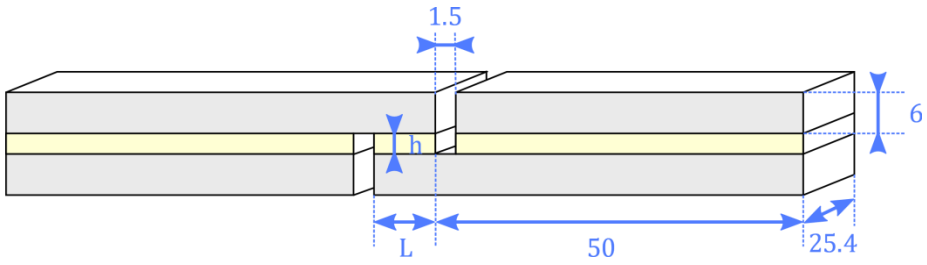

Figure 2: Thick Adherent Shear Test (TAST) geometry. Dimensions are given in millimeters.

2.3. ARCAN test

The ARCAN geometry adapted to adhesive testing consists in a butterfly shape illustrated in Figure 3, with two holes in each substrate that permits to fix the specimen to a special fixture device. This way, the loading is imposed close to the joint and not at the extremity of the substrate, away from the joint. The positions of the holes, coupled to the geometry of the substrates, are supposed to prevent any spurious bending of the assembly. No standard describes this method, therefore the Figure 3 gives a general drawing of the ARCAN geometry concept with dimensions chosen according to typical values (in millimeters) found in the literature.

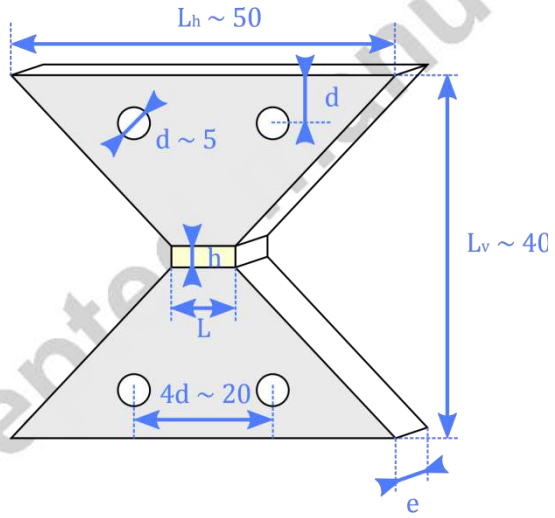

Figure 3: ARCAN geometry. Typical dimensions are given in millimeters.

Several conditions between the dimensions of the geometry should be respected to avoid any unexpected effects, more specifically:

- $L_h \geq 5L$ and $L_v \sim L_h - L$: this condition permits to keep the global geometric aspect of the specimen and avoid angles far away from $45°$ and $135°$ for the substrate shape
- $d \leq L_v/8$: this condition ensures that the clamping holes are not too close to the joint, which would deteriorate the loading homogeneity in the joint as the Saint-Venant approximation no longer applies

2.4. Napkin Ring test

The Napkin ring geometry has a cylindrical symmetry as illustrated on Figure 4 and is therefore configured for a twist loading. It consists in two metallic rings bonded together by the joint, which has therefore the same inner and outer radius as the rings. Holes in the ring substrates, away from the joint, allow the assembly to be fixed to a twisting machine with a specific device.

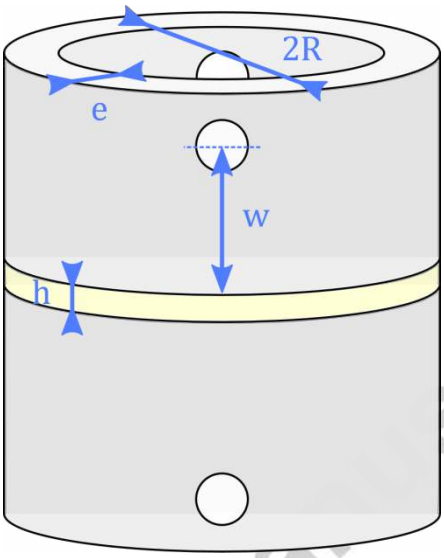

Figure 4: Napkin ring geometry

This method is not described in the actual standards. Therefore, there is no absolute value for the dimensions to be given but rather some relations between the parameters to be respected:

- $e \leq R/5$: this condition ensures stress homogeneity in the radial direction. The joint transverse area then reads $S \approx 2\pi Re$
- $w \geq 5R$: this condition ensures that the Saint-Venant approximation applies (the stress state of the joint does not depend on the clamping conditions on the holes)

3. Notations and modeling assumptions

For the SLJ, TAST and ARCAN configurations, the joint under scrutiny is modeled with a rectangular shape (see Figure 5 (a)): the joint length L is aligned with the $\underline{e}_1$ direction, the joint thickness h corresponds to the $\underline{e}_2$ direction and the joint width w is taken in the last $\underline{e}_3$ direction, where $\underline{e}_1$, $\underline{e}_2$ and $\underline{e}_3$ denote the unit coordinate vectors of a Cartesian coordinate system.

The origin of the space description is taken at the joint bottom left corner, which means the joint occupies the space region $0 \leq x \leq L$; $0 \leq y \leq h$; $0 \leq z \leq w$.

The specimen is loaded under simple shear stress σ_{12}, symbolized by the red arrows on Figure 5 (a). However as will be further discussed, this is only the main solicitation in the adhesive joint and further spurious components will be generated by the specific geometry of the specimen.

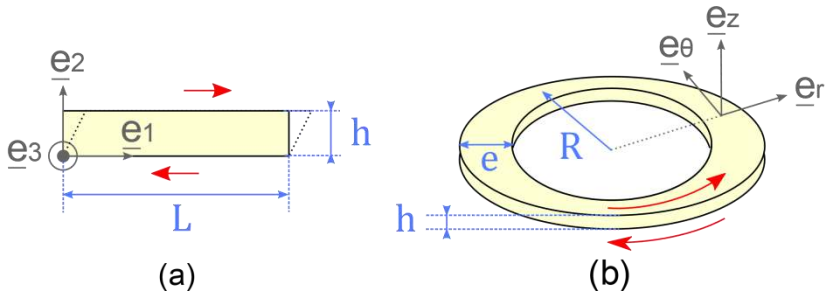

Figure 5: Space conventions for SLJ, TAST and ARCAN (a), and napkin ring (b). The red arrows symbolize the shear loading induced in the joint during solicitation

The joint geometry of the napkin test specimen where axial symmetry is assumed is illustrated on Figure 5 (b): the joint thickness h is oriented in the $\underline{e_z}$ direction and joint width e in the $\underline{e_r}$ direction, where $\underline{e_r}$ and $\underline{e_z}$ denote the unit coordinate vectors of a Cylindrical coordinate system.

The joint length L has a period of $2\pi R$, R being the radius of the ring. With this convention, the joint occupies the space region $-e/2 \leq r \leq R + e/2$; $0 \leq \theta \leq 2\pi$; $0 \leq z \leq h$.

The loading of the napkin ring sample is supposed to induce as the main solicitation a shear stress $\sigma_{\theta z}$ illustrated with the red arrows.

The thickness was set to $h = 1\ mm$ in all the computations presented in this paper, and the length L was varied between $10\ mm$ and $100\ mm$. The thickness to length ratio h/L varies as a consequence from 10^{-1} to 10^{-2}. The reader is referred to Appendix A for more information on the influence of the thickness of the joint on its mechanical state during solicitation.

Most of the adhesive joints are constituted of polymer components and will exhibit a viscoelastic material behavior. However, in order to estimate the spatial distributions of strains and stresses, the materials will be considered linear elastic. This is a consequence of a time space separation of variables at the considered time scales. Further justifications based on an example about modeling viscoelastic materials with elastic constitutive laws is given in Appendix B.

The parameters of the substrate and the joint are denoted with subscript 1 and subscript 2 respectively. . The main discussion is based on aluminum substrates with a Young modulus $E_1 = 70\ GPa$ and a Poisson coefficient $\upsilon_1 = 0.33$ and nearly incompressible adhesive joints with shear modulus $G_2 = 100\ MPa$ and a Poisson coefficient $\upsilon_2 = 0.49$. This value of the joint shear modulus G_2 was chosen because it lies in the middle of the typical range of adhesive stiffness: indeed, the order of magnitude of stiff thermoset adhesives like poyimide or epoxy is about 1 GPa, whereas the order of magnitude of flexible adhesive like silicone a thousand times smaller, i.e. about 1 MPa. Given the chosen values in this study, the adhesive joint to substrate stiffness ratios are of $E_2/E_1 = 4.3 \times 10^{-3}$ if expressed in term of the Young

moduli and of $G_2/G_1 = 3.8 \times 10^{-3}$ when expressed in terms of the shear moduli. This configuration corresponds therefore to configurations where substrates are much stiffer than the adhesive layer.

For illustrative purposes, the Table 1 displays typical stiffness ratios for different adhesives and adherents (substrates). One can remark that the stiffness ratio can vary over 5 orders of magnitude between 1 and 10^{-5}.

Table 1: Joint over substrate stiffness ratios for typical material combinations

	Polycarbonate $E_1 = 2.3\ GPa$	Aluminum $E_1 = 70\ GPa$	Steel $E_1 = 210\ GPa$
Silicon based adhesive $E_2 = 1\ MPa$	$E_2/E_1 \sim 5 \cdot 10^{-4}$	$E_2/E_1 \sim 1.5 \cdot 10^{-5}$	$E_2/E_1 \sim 5 \cdot 10^{-6}$
Epoxy resin $E_2 = 3.5\ GPa$	$E_2/E_1 \sim 1.5$	$E_2/E_1 \sim 5 \cdot 10^{-2}$	$E_2/E_1 \sim 1.5 \cdot 10^{-2}$

The shear properties of the joint are computed from the measured applied load, which is actually the resultant force F (for SLJ, TAST and ARCAN setups) or moment M (for the napkin ring method), and the estimated relative displacements of the extremity of both substrates.

In the following, the focus is made on the normalized local shear stress τ_n defined as the local shear stress $\sigma_{12}(x,y) = \tau(x,y)$ divided by the average shear stress $\overline{\tau}$ within joint. The normalized local shear stress τ_n is a good illustration of the spatial heterogeneity of the stresses in the adhesive joint. Table 2 displays the expression of $\overline{\tau}$ and τ_n using the conventions and dimensions presented in the Figure 5:

Table 2: Expressions of $\overline{\sigma}$ and τ for all testing methods

SLJ / TAST / ARCAN	Napkin ring
$\bar{\tau} = F/S$ with $S = Lw$	$\bar{\tau} = M/RS$ with $RS \approx 2\pi R^2 e$
$\tau_n(x,y) = \dfrac{\sigma_{12}(x,y)}{\bar{\tau}} = \dfrac{\sigma_{12}(x,y)}{F/Lw}$	$\tau_n(\theta,z) = \dfrac{\sigma_{\theta z}(\theta,z)}{\bar{\tau}} = \dfrac{\sigma_{\theta z}(\theta,z)}{M/2\pi R^2 e}$

In this context, the average shear stress $\overline{\tau}$ has the dimension of a stress, whereas the normalized shear stress τ_n is dimensionless.

Next the hydrostatic stress σ_p and the equivalent stress σ_{eq} are classically defined as

$$\sigma_p = \frac{1}{3}\mathrm{tr}\left(\underline{\underline{\sigma}}\right)$$

$$\sigma_{eq} = \sqrt{\frac{3}{2}\left(\underline{\underline{\sigma}} - \sigma_p \underline{\underline{I}}\right) : \left(\underline{\underline{\sigma}} - \sigma_p \underline{\underline{I}}\right)}$$

with $\underline{\underline{\sigma}}$ the Cauchy stress tensor, and $\underline{\underline{I}}$ the second order identity tensor. The reader is referred to Appendix C for more detailed expressions of σ_p and σ_{eq}.

The triaxiality ratio is introduced as the ratio between the hydrostatic stress and the equivalent stress:

$$T = \frac{\sigma_p}{\sigma_{eq}}$$

The Table 3 gives the theoretical values of the triaxiality ratio for the characteristic mechanical states, including 95%-confidence intervals when adding 10% random noise on all components of the stress tensor:

Table 3: Triaxiality ratio values and dispersion for typical mechanical states

State	Triaxiality ratio theoretical value	Confidence interval
Pure shear	$T = 0$	$[-0.037\ ;\ 0.037]$
Uniaxial tension	$T = 1/3$	$[0.257\ ;\ 0.410]$
Uniaxial compression	$T = -1/3$	$[-0.410\ ;\ -0.257]$
Isotropic tension	$T = +\infty$	$[3.96\ ;\ +\infty[$
Isotropic compression	$T = -\infty$	$]-\infty\ ;\ -3.96[$

The joint is supposed to be loaded in simple shear during the test. Hence the two criteria retained in this study are:

- The deviation of the normalized shear stress from its theoretical value $\tau = 1$. This criterium indicates if the geometry is suitable for a characterization test of the adhesive joint mechanical behavior, where stress homogeneity is of importance.
- The triaxiality ratio deviation from its theoretical value $T = 0$. This criterion determines whether fatigue testing would effectively lead to failure due to shear stress instead of potential tensile stresses.

In order to access the local stress and strain fields, a detailed computation with the Finite Element Method is used. The computations were performed with the ABAQUS software under plane strain and small strains assumptions for the first three standards (SLJ, TAST and ARCAN tests), which corresponds to the joint state at mid-width $z = w/2$. This choice implies that $\sigma_{13} = \sigma_{23} = 0$ and $\sigma_{33} = \nu_i(\sigma_{11} + \sigma_{22})$ where the indexes $i = 1{,}2$ denote the substrates and the adhesive joint respectively.

Quadratic rectangular elements with reduced integration CPE8R are used for all the substrates, whereas elements with a hybrid formulation CPE8RH were chosen for the joints to handle more easily the quasi-incompressibility ($\nu_2 = 0.49$) of the adhesive material. The mesh is particularly refined at every joint edge in order to capture brutal changes of the fields near the interfaces. A minimum of twenty elements across the thickness are necessary to quantitatively capture the stress and strain concentrations. However, it is not consistent to refine the mesh more than the tolerance of the dimensions. Typically, element sizes below 10 microns on the free edges of the joint are likely to be unrealistic because guarantying the joint edges shape at such a precision is experimentally very difficult. Some adhesives are

also filled with particles, such that they cannot be considered homogeneous any more at the filler length scale. Refining the mesh more than that length scale is therefore non-consistent with the assumptions of material homogeneity inside an element of the mesh. In addition, the number of elements in the thickness direction of the substrates should be enough to catch their potential bending, typically six to ten elements are needed. As an example, the Figure 6 shows the mesh used for the FEM computations of the single lap shear assembly in the joint area, with a zoom at a joint corner to show the mesh refinement at the joint edges. Other geometries were meshed similarly.

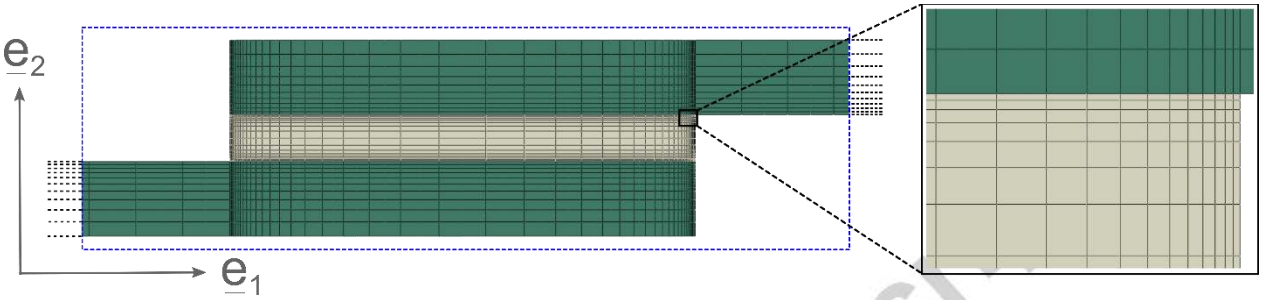

Figure 6: Rectangular quadratic mesh of the SLJ bonded assembly in the joint area, with a zoom at the joint corner. The mesh was refined near the interfaces. The smallest element size is $10\ \mu m$.

The boundary conditions are formulated in displacement

- Clamping, i.e. ***imposed zero displacements*** $\underline{\boldsymbol{u}} = \underline{\mathbf{0}}$, on the left extremity of the SLJ and the TAST and on the holes of the lower substrate of the ARCAN geometry. As $\underline{u} = \underline{0}$ is imposed on a segment it follows that no rotations are permitted on the boundary. Moreover, the mesh consists of volumetric elements and therefore no rotational degrees of freedom are included in the model as would be the case for a thin shell element.
- ***Imposed displacement*** $\underline{\boldsymbol{u}} = \boldsymbol{d}\underline{\boldsymbol{e}}_{\boldsymbol{1}}$ on the right extremity of the SLJ and the TAST and on the holes of the upper substrate of the ARCAN geometry. Rotation is prevented for the same reasons as for the clamping on the other substrate.

The Figure 7 represents the deformed state of the bonded assemblies under loading: the shear strain $\gamma_{12} = 2\varepsilon_{12}$ normalized by the macroscopic imposed strain $\gamma_0 = d/h$ has been plotted. The quantity γ_0, defined as the macroscopic imposed strain, actually corresponds to the average strain in the joint if substrates were completely rigid. The boundary conditions in displacement are illustrated with red symbols on this Figure 7. In order to emphasize any substrate deformation, all deformed states were plotted with $d = 2h$ (i.e. $\gamma_0 = 2$). Deformation scale factors were set to 1 to be able to qualitatively compare the behavior of each method.

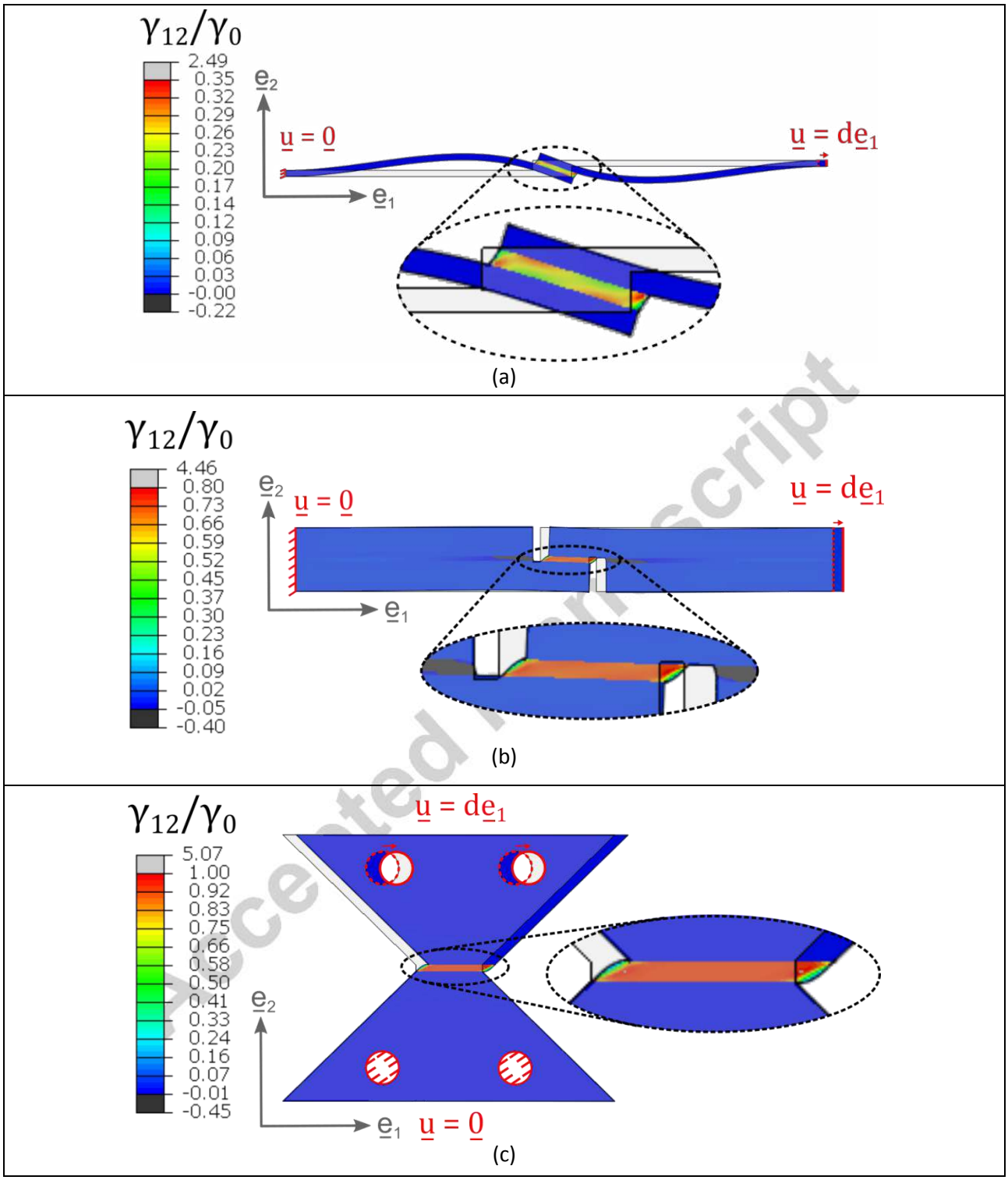

Figure 7: Deformed states for $\gamma_0 = d/h = 2$ with a zoom on the joint area for the SLJ (a), the TAST (b) and the ARCAN (c). The color scales correspond to the normalized shear strain γ_{12}/γ_0

Qualitative differences can be already noticed:

- The TAST and ARCAN joints are closer to homogeneous state than the lap shear joint.

- The substrates of the lap shear setup are highly bent, whereas their bending is very limited in the TAST configuration and eliminated for the ARCAN geometry.
- The normalized shear strain is somewhat smaller than 1 especially for the SLJ method, meaning the deformation of the substrates cannot be neglected in spite the very low joint to substrate stiffness ratio.

The absence of symmetry of the loading for the napkin ring imposed the usage of a complete 3D geometry for the analysis of this test. The small strains assumption is considered here. The dimensions chosen are:

- $R = 5.5\ mm$
- $e = 1\ mm$
- $w = 5\ mm$

The second condition $w \geq 5R$ of the napkin ring method was consciously not verified in this study. Its physical significance is that the Saint-Venant approximation generally used for slender objects like rods and plates is not verified in this situation. In this case, it implies that homogeneity of the mechanical state in the joint can be degraded by the proximity of the clamping holes.

To get a precise and consistent stress and strain state within the joint, the mesh was refined in order to reach seven elements in the axial direction and twenty elements in the radial direction as illustrated on Figure 8 (b). The elements used in the joints are hexahedral quadratic, with a reduced integration and a hybrid formulation: C3D20RH. The substrates are meshed with tetrahedral quadratic elements with a modified formulation C3D10M. Tie constraints are applied at the joint and substrates facing surfaces to make them integrals.

Boundary conditions are here expressed in terms of an imposed rotation angle α at the level of the clamping holes of the upper substrate, the holes of the lower one being clamped:

- $\underline{u} = \underline{0}$ on the holes of the lower substrate, any rotation prevented
- $\underline{u} = \alpha R \underline{e_\theta}$ on the holes of the upper substrate

As for the three other geometry models exposed previously (SLJ, TAST, ARCAN), this macroscopic loading parameter α permits to define the quantity $\gamma_0 = \alpha R/h$ as the macroscopic imposed strain. The Figure 8 (a) presents the deformed state of this test configuration, where the colors denote zones of equal normalized shear strain $\gamma_{\theta z}/\gamma_0$. Boundary conditions in displacement are illustrated with red symbols. The Figure 8 (c) shows a zoom on the deformed shape of the joint in sectional view. The two following qualitative remarks can be made:

- the shear strain is not totally homogeneous as well and does not seem to be completely θ-independent (14% variation). This θ-dependence is a consequence of the violation of the $w \geq 5R$ condition.
- the normalized shear strain is once again smaller than 1 (about 0.28), which induces that the substrates deformation has to be taken into account

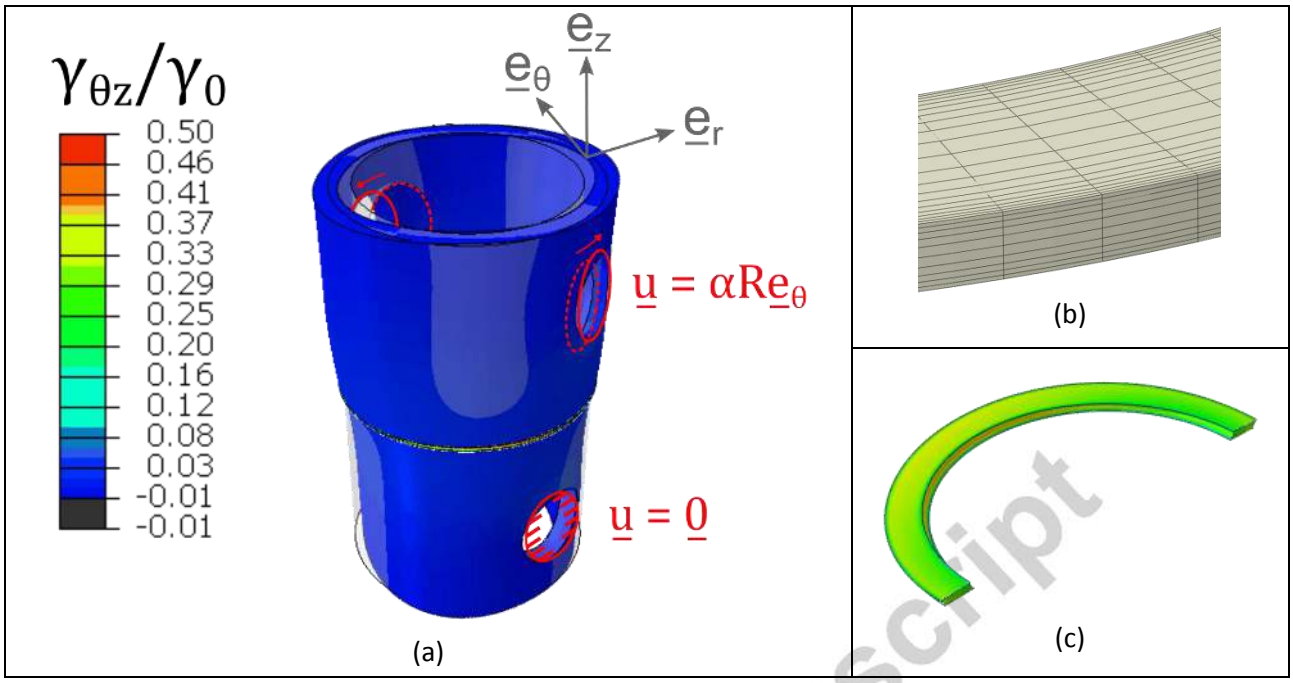

Figure 8: FEM computation of the napkin ring geometry: normalized shear strain in bonded sample (a), joint mesh (b), deformed shape of the joint in sectional view. The color scale corresponds to the one of part (a) of the figure.

4. Evaluation of stress singularities at joint-substrate interfaces

At the corner of the joint and the substrate (see Figure 9 for the local geometry simplification), geometrical and material discontinuities are encountered which lead to potential stress and strain singularities. The singularity only affects a local neighborhood of the material discontinuity. It reflects at a rather local scale the geometric detail of the test configuration, and does therefore not depend of the complete test geometry.

The three main parameters characterizing the problem are:

- the joint over substrate stiffness ratio E_2/E_1, or similarly expressed as G_2/G_1
- the local substrate angle δ_1
- the local joint angle δ_2

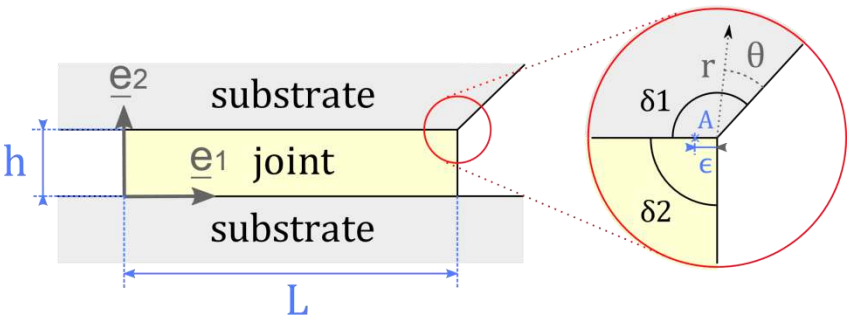

Figure 9: Joint-substrate local interface geometry

The outcome of stress singularities is classically known as the Williams eigenfunction analysis (see). The phenomena can be understood by analyzing the asymptotic behavior of the displacement solution using the polar coordinates (r, θ) with origin at the joint corner. Stress and displacement fields are assumed to have the following form :

$$\begin{cases} \underline{\underline{\sigma}}(r,\theta) = r^{\lambda-1}\underline{\underline{F}}(\theta) \\ \underline{u}(r,\theta) = r^{\lambda}\underline{G}(\theta) \end{cases} \quad (1)$$

Both functions $\underline{\underline{F}}(\theta)$ and $\underline{G}(\theta)$ designate bounded and continuous with respect to θ. The reader has to remind that they also implicitly depend on the local geometry δ_1 and δ_2. This implies in particular that displacement jumps between joint and substrate are prohibited (the joint-substrate interface is considered fully and perfectly glued).

The displacement remains bounded in the vicinity of the wedge as $r \to 0$ if and only if $\lambda > 0$. This condition assures that the strain-energy $1/2\left(\underline{\underline{\sigma}} : \underline{\underline{\nabla}}(\underline{u})\right) r\mathrm{d}r\mathrm{d}\theta$ has a bounded value.

A stress singularity occurs if $\lambda < 1$: in this case the stress tensor has the form $\underline{\underline{\sigma}} = \frac{1}{r^{1-\lambda}}\underline{\underline{F}}$ with $1 - \lambda > 0$ which diverges for $r \to 0$.

An analytical study based on was first conducted considering the substrate as totally rigid compared to the joint, i.e. $E_2/E_1 = 0$. As the substrate does not deform, the results become independent of its local shape δ_1. The joint boundary conditions in displacement for this case simply read in the Cartesian reference basis defined in section 3 (and illustrated Figure 9):

$$\begin{cases} \underline{u}(0 < x < L, y = 0) = \underline{0} \\ \underline{u}(0 < x < L, y = h) = d\underline{e}_1 \end{cases}$$

The horizontal edges of the joint (defined by $y = 0$ or $y = h$) are considered to be clamped by the substrates whereas the vertical ones ($x = 0$ ou $x = L$) remain stress free. The evolution of the eigenvalue λ with the joint angle δ_2 under these boundary conditions is illustrated in Figure 10 for three different values of joint Poisson's ratio.

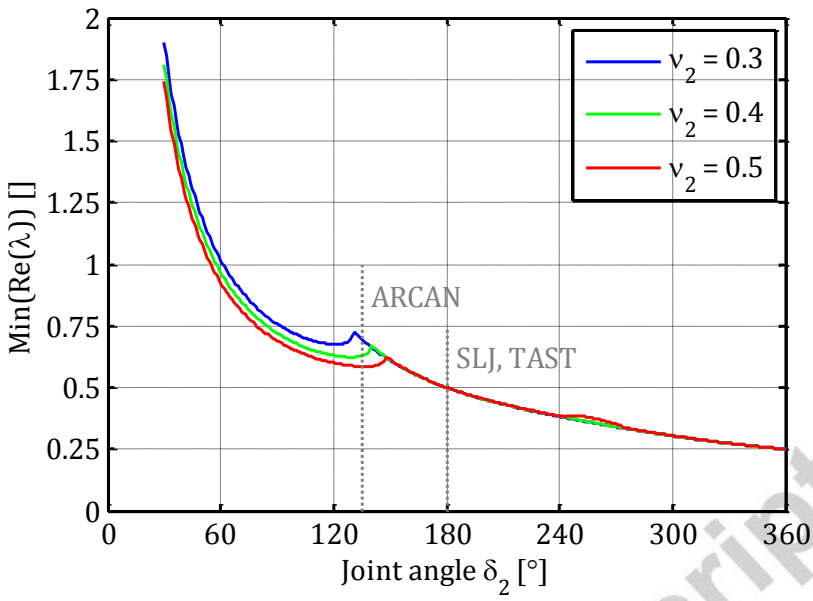

Figure 10: Singularity eigenvalue λ in function of the joint angle δ_2 for three different values of the joint Poisson's ratio ν_2

The singularity appears for incompressible materials like rubbery joints ($\nu_2 = 0.5$) for $\delta_2 > 54°$. Concerning stiffer adhesives like epoxy or polyimide joints that have a smaller Poisson's ratio (about $\nu_2 = 0.35$), stress singularity arises for $\delta_2 > 60°$.

The consequences of the change of the singularity exponent λ with the joint angle δ_2 will be detailed with numerical FEM computations for $\delta_2 \in [30°; 90°]$.

Table 4: FEM shape for $\boldsymbol{\delta_2 \in [30°; 90°]}$

δ_2	30°	45°	60°	75°	90°
FEM shape	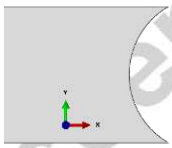	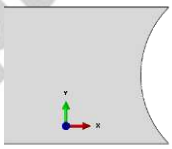	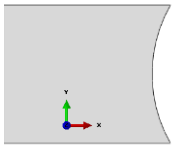	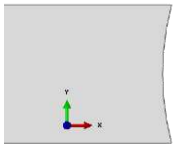	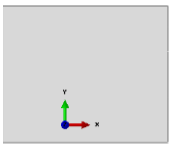
λ ($\nu_2 = 0.5$)	1.74	1.18	0.92	0.78	0.69

The conditions of the FEM computations are identical to those used in the previous part: 2D plane strain and small strains assumptions. The joint is here also meshed with quadratic rectangular elements with reduced integration and hybrid formulation CPE8RH. The mesh was refined near its edges. This study pretends to deal with edge effects at the joint interfaces (and corners) independently of the geometry of the substrates. Therefore, the substrates will not be modelled here, but the boundary conditions will be directly applied on the joint interfaces instead. This choice is equivalent to considering that the substrates are completely rigid. The applied boundary conditions read this time:

- Clamping $\underline{u} = \underline{0}$ on the lower interface, no rotation allowed
- Imposed horizontal displacement $\underline{u} = d\underline{e_1}$ on the upper interface, no rotation allowed

The Figure 11 shows the mesh used for this analysis with a zoom on the upper right corner to illustrate the joint angle δ_2 . The boundary conditions are illustrated with red symbols.

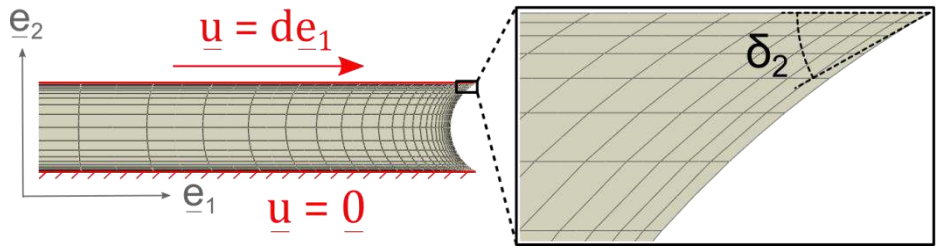

Figure 11: Mesh of a half of the joint for the configuration $\delta_2 = 30°$, with a zoom on the joint upper right corner. The angle is defined on the zoom part. Boundary conditions are illustrated in red.

The case of elastic substrates ($E_2/E_1 > 0$) is then addressed. The singularity zone in the plane (δ_1, δ_2) for different values of E_2/E_1 is theoretically explored based on (see Appendix D for more details on the mathematical derivations). The results are displayed in Figure 12: the different curves represent the delimiting curve between the regular zone ($\lambda \geq 1$) and the singularity zone ($\lambda < 1$) for the mentioned stiffness ratios.

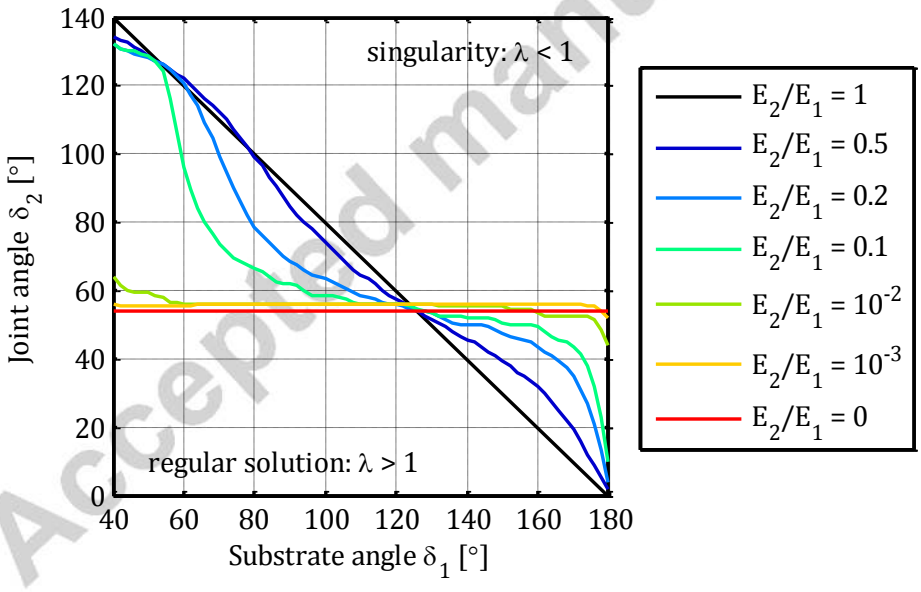

Figure 12: Map of regular and singular areas function of joint and substrate angles δ_1 and δ_2

The curve delimiting the two areas progressively evolves from $\delta_1 + \delta_2 = 180°$ for $E_2 = E_1$ (homogeneous joint-substrate assembly) to $\delta_2 = 54°$ for $E_2/E_1 = 0$ (rigid substrates). Sharpening both angles (including the substrate angle δ_1) is therefore the best way to avoid any stress singularity at joint corner.

5. Numerical results

This section presents the quantitative results and the comparison of the different setups. The focus is brought on the spatial distribution of both normalized shear stress τ_n and triaxiality ratio T in two distinct locations within the joint: its middle plane defined by $y = h/2$ and its two interfaces with the substrates defined by $y = 0$ or h.

5.1. Shear stress homogeneity and triaxiality ratio at joint mid-plane $y = h/2$

In this paragraph, all results were obtained with the material parameters given in part 3: $E_1 = 70\ GPa$, $\upsilon_1 = 0.33$ for the substrates and $G_2 = 100\ MPa$, $\upsilon_2 = 0.49$ for the adhesive joint The y coordinate is set to $h/2$ and the x coordinate describes the entire joint, i.e. $x \in [0\ ;\ L]$. This is equivalent to discuss the results in terms of the reduced coordinate x/L, which runs through $[0\ ;\ 1]$. As the height is fixed, all fields therefore only depend on x or equivalently on x/L.

Figure 13 presents the evolution of the normalized shear stress $\tau_n(x/L)$, and the evolution of the triaxiality ratio $T(x)$ within joint half-length (the evolution is actually symmetric for the other half of the joint) for the SLJ method:

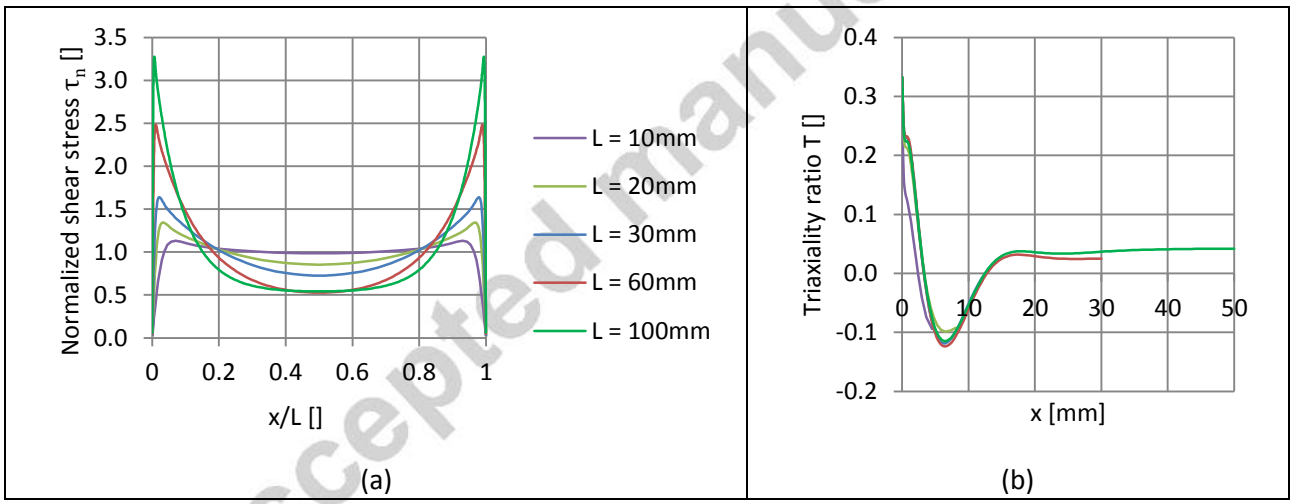

Figure 13: Shear stress repartition (a) and triaxiality ratio (b) at joint mid-plane for the SLJ method

The shear state becomes more heterogeneous as the joint length L is extended: the extremities are increasingly loaded at the expense of the middle of the joint, which is a serious limit for a characterization test. The Table 5 shows the ratio of the maximum shear stress over the shear stress in the middle of the joint $x = L/2$:

Table 5: Maximum over middle shear stress ratio for SLJ

$L\ (mm)$	10	20	30	60	100
$\frac{\tau_n^{max}}{\tau_n^{L/2}}$	1.147	1.573	2.259	4.207	6.209

On the other hand, the triaxiality ratio has the same behavior at joint extremity whatever the joint length. The triaxiality value at joint ends $T(x = 0 \text{ or } L)$ is about 0.34 and therefore corresponds to a uniaxial tension instead of a pure shear, meaning that a fatigue failure would appear because of tensile stresses rather than shear stresses. These tensile stresses are actually due to the bending phenomenon of the substrates illustrated on the deformed shape of the specimen (see Figure 7).

The results for the TAST setup and comparison with the lap shear test are presented in Figure 14 for two different joint lengths: $10\ mm$ and $30\ mm$. It is recalled here that the overlap length for the TAST geometry is supposed to be $10\ mm$, and the results for $30\ mm$ are given here only as an illustration of the influence of long overlaps for this geometry.

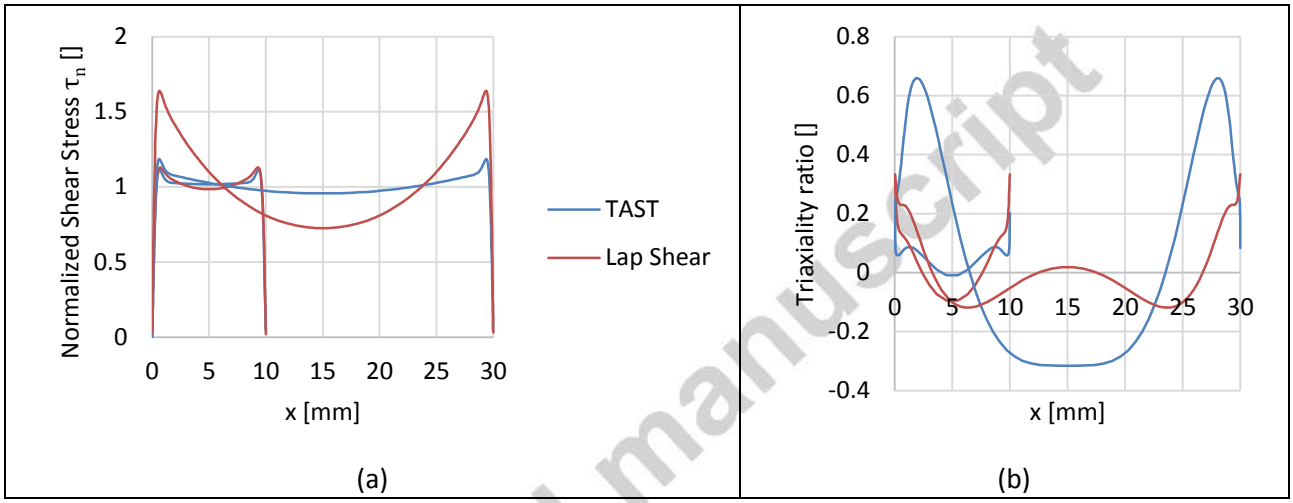

Figure 14: Shear stress repartition (a) and triaxiality ratio (b) at joint mid-plane for the TAST and SLJ methods for two distinct joint lengths: $L = 10\ mm$ and $30\ mm$

Table 6 of $\tau_n^{max}/\tau_n^{L/2}$ ratios is dressed for the TAST method where the values obtained with the single lap shear test are also recalled for comparison purposes:

Table 6: Maximum over middle shear stress ratio for SLJ and TAST

$L\ (mm)$	10	30
$\left(\frac{\tau_n^{max}}{\tau_n^{L/2}}\right)_{SLJ}$	1.147	2.259
$\left(\frac{\tau_n^{max}}{\tau_n^{L/2}}\right)_{TAST}$	1.093	1.238

Shear stress τ_n homogeneity is improved with the TAST geometry compared to the lap shear test, especially for lengths larger than $30mm$ where the single lap shear was already poor: the $\tau_n^{max}/\tau_n^{L/2}$ ratio is reduced by 45% for the TAST compared to the lap shear at $L = 30\ mm$. This improvement is a consequence of increasing the substrate thickness, which strengthens its bending stiffness. Nevertheless, this thickness increase also leads to a triaxiality rise enhanced when increasing the joint length: the

triaxiality ratio reaches indeed 0.66 for $L = 30\ mm$, which is twice as high as for the lap shear setup. It is clear here that increasing the thickness of the substrate (form SLJ to TAST) induces a completely different behavior for the triaxiality ratio distribution. The TAST can therefore not be simply considered as a "better" single lap shear test with thicker substrates. These high triaxiality values appear because the vertical movement (in the $\underline{e_2}$ direction) due to slight bending of the substrates of the TAST is not totally prevented regardless of their thickness. The TAST method is therefore a good candidate for a behavior characterization test, but must be used with care if for a fatigue test because early failures could outcome from this high triaxiality value involving high normal stresses.

The Figure 15 presents the shear stress τ_n and the triaxiality ratio T in a $10\ mm$-long ARCAN joint with the previous TAST and lap shear plots superimposed for comparison:

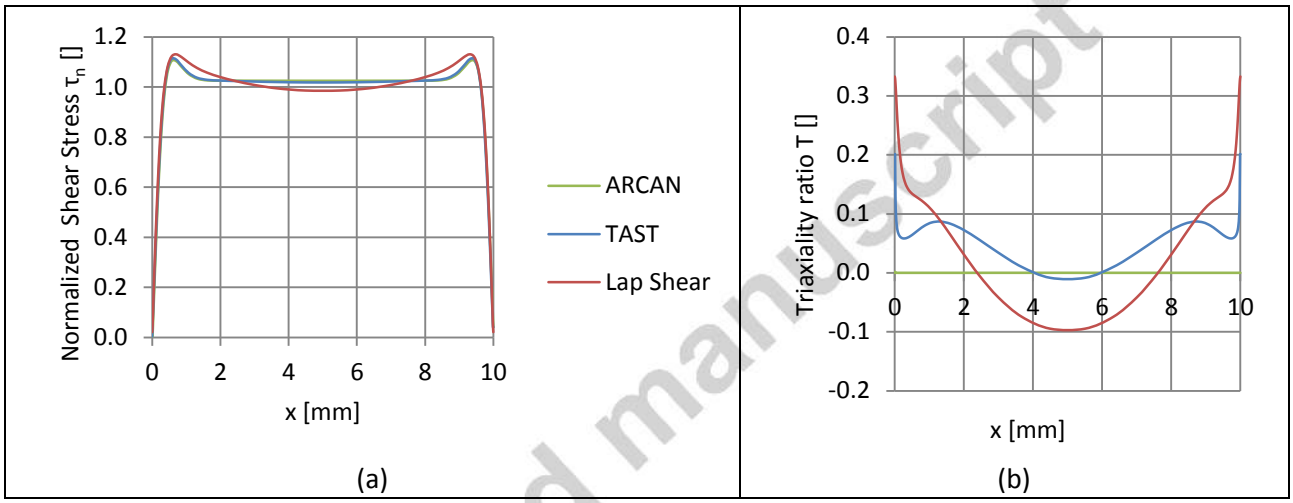

Figure 15: Shear stress repartition (a) and triaxiality ratio (b) at joint mid-plane for the ARCAN method, superimposed with TAST and SLJ results for $L = 10\ mm$

The stress homogeneity for both ARCAN and TAST setups are nearly identical (less than 1% deviation between the two curves). However, a light peak is noticed about $\tau_n = 1.1$ near joint extremities, which is present for the ARCAN as well as for the TAST method. This peak compensates the sudden stress drop at the free edges of the joint $x = 0$ or L and seems therefore unavoidable. But this time, the triaxiality ratio reaches 0 ± 10^{-3}, i.e. the stress state at joint mid-plane for the ARCAN method can be considered as pure shear. This result was moreover obtained for any joint length L in the interval of interest for the study $[10mm\ ; 100mm]$. This phenomenon could be explained by the fact that the imposed boundary conditions on the ARCAN geometry eliminates any potential bending movement of the substrate, preventing any rise of normal stresses because substrate are structurally much stiffer in tension/compression.

Results for the last napkin ring method are shown in Figure 16, together with the three previous methods for comparison purposes. The convention chosen here for the joint length L is $L = 2\pi R$, R being the ring radius.

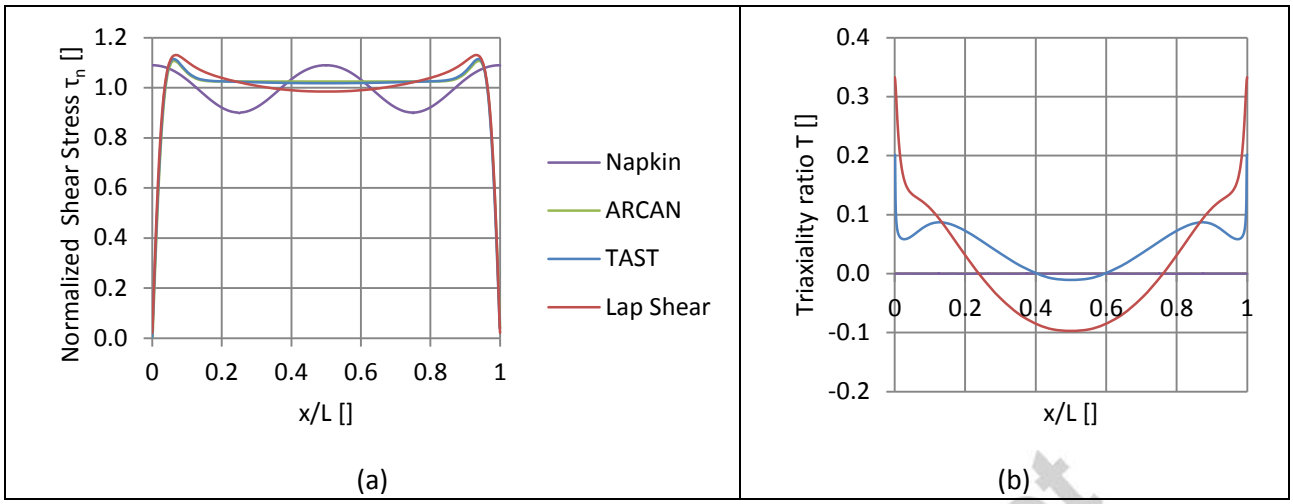

Figure 16: Shear stress repartition (a) and triaxiality ratio (b) at joint mid-plane for the napkin ring method, superimposed with the three other methods for $L = 10\ mm$

If the free ends of the lap shear, TAST and ARCAN joints inevitably imply a sudden drop of the shear stress, the napkin ring specimen does not present this inconvenience: any stress drop at joint ends and the associated peaks near the extremities have disappeared. Nonetheless, shear stress oscillation appears, related to the clamping boundary conditions if the holes in the substrates are not far enough away from the joint. This illustrates the role of the second condition $w \geq 5R$, which makes this parasitic oscillation progressively vanish as the holes are moved away from the joint. The triaxiality ratio remains about 0 ± 10^{-4}, as close to 0 as for the ARCAN geometry and for the same reason (no substrate bending permitted).

A series of experimental results obtained with all the previously exposed methods is exposed in and the references therein. One can remark that they lead to non-linear material behavior. The numerical response of a non-linear adhesive under a monotonic shear test with the four geometries is now analyzed: *(i)* substrate modelling is as above, *(ii)* the joint has a non-linear behavior modeled using an elastoplastic formulation with a classical von Mises yield criterion and an isotropic hardening in the ABAQUS software:

$$\underline{\underline{\varepsilon}} = \underline{\underline{\varepsilon}}^e + \underline{\underline{\varepsilon}}^p$$

and

$$\begin{cases} \underline{\underline{\sigma}} = \underline{\underline{\underline{\underline{C}}}} : \underline{\underline{\varepsilon}}^e = \underline{\underline{\underline{\underline{C}}}} : \left(\underline{\underline{\varepsilon}} - \underline{\underline{\varepsilon}}^p\right) \\ f\left(\underline{\underline{\sigma}}, q\right) = \sigma_{eq} - \left(\sigma_0 + R(q)\right) \leq 0 \\ \dot{\underline{\underline{\varepsilon}}}^p = \lambda \dfrac{\partial f}{\partial \underline{\underline{\sigma}}} \quad and \quad \lambda f = 0 \\ \dot{q} = -\lambda D \dfrac{\partial f}{\partial q} \end{cases}$$

For the computations presented here, a stress-strain relation inspired by the experimental data of the 1-part epoxy Ciba AV119. The constitutive law represents an average of the experimental results in the figure 10 of , and is displayed as a black dotted curve on Figure 17. Additional information on the experimental conditions can be found in and . The relatively large shear modulus of this adhesive at small strains $G_{material} = 1075\ MPa$ of the simulated adhesive when compared to typical adhesive stiffness in Table 1 permits to highlight any difference between the four shear tests. The isotropic hardening $R(q)$ is entered in the software as a tabular input, which implies its piecewise-linearity. The asymptote at large strain is horizontal. The tabular data of $R(q)$ is given in appendix E.

The values of stress and strain discussed next are numerically computed as follows:

- the mean shear stress $\overline{\tau}$ is computed according to the expressions in Table 2
- the mean shear strain $\overline{\gamma}$ is defined as δ/h with h being the joint thickness and δ the relative displacement between the two joint-substrate interfaces, taken at the middle of the joint overlap. This latter quantity δ can be experimentally measured either by reading on a strain gauge or using DIC.

The Figure 17 shows the response curves computed with ABAQUS® for the lap shear, the TAST, the ARCAN and the napkin ring tests, with a zoom in the small strains regions ($\bar{\gamma} \leq 0.1$) on the right side. The overlap length for the first three methods was set to $L = 10\ mm$. The computations are stopped once the stress asymptote was considered reached. The extremities of the plots therefore do not reflect any specimen or material failure, but only the end of the computations.

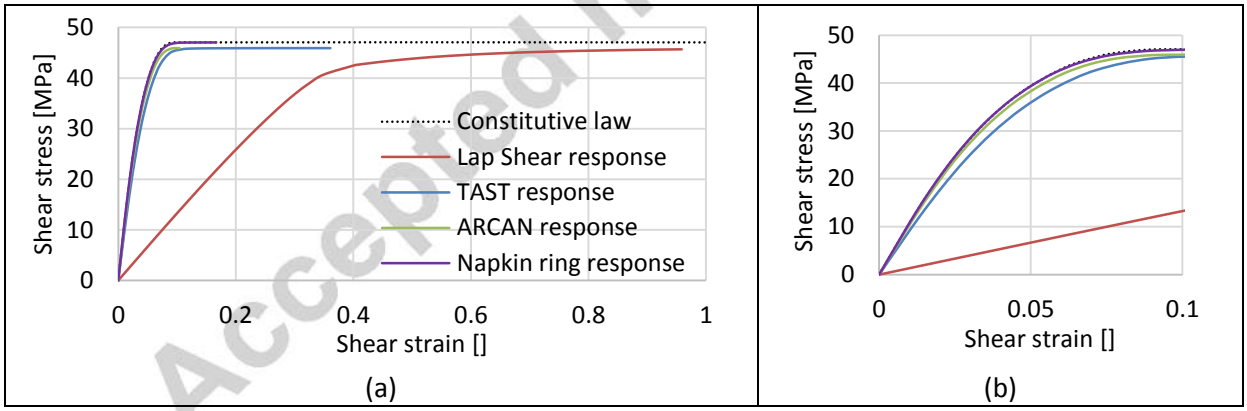

Figure 17: Comparison of the mean shear stress-strain response using different experimental setups for the whole strain range explored (a) and a zoom for strains smaller than 0.1 (b). The shear stress was numerically determined from the macroscopic load or torque, whereas the shear strain was numerically determined form the relative displacement of the opposite interfaces of the joint at the middle of its overlap.

The strong limitations of the SLJ configuration are noticed here, where the shear modulus at small strains $G_{SLJ} = 133\ MPa$ is actually one order of magnitude smaller than the material modulus $G_{material}$. The TAST curve is a lot closer to the material one and gives $G_{TAST} = 918\ MPa$, i.e. an underestimation of 15%. The ARCAN test fits reasonably the small strain behavior with $G_{ARCAN} = 1043\ MPa$ ($i.e.\ 3\%$ underestimation) and starts to get away from the material curve only when reaching high stress levels. At last, the napkin ring curve fits perfectly the material behavior with less than 1% difference between the two curves on the whole strain range explored. These curves are of course the results of simple

numerical computations instead of true experimental tests. Nonetheless, they clearly permit to discriminate the four test methods studied in this paper in terms of evaluation of both shear modulus in the small strain range and non-linear hardening in the finite strain range, with respect to the constitutive law used as input.

5.2. Shear stress homogeneity and triaxiality ratio at joint and substrate interface $y = 0$ or $y = h$

In this paragraph, numerical computations were carried out to characterize the potential stress singularity at the joint corners depending on the joint angle δ_2, for $\delta_2 \in [30°; 90°]$ (see Figure 9) in that specific case of totally rigid substrates $E_2/E_1 = 0$. The material parameters of the joint are the same as in the previous paragraph: $G_2 = 100\ MPa, \upsilon_2 = 0.49$.

The evolution of the simple shear stress σ_{12}, the equivalent stress σ_{eq} and the hydrostatic stress σ_p (all normalized by the average shear stress $\bar{\tau} = F/S$) with respect to the joint angle δ_2 is noted at a point $A(x = L - \varepsilon, y = h)$ lying on the joint-substrate interface closed to the joint corner illustrated on Figure 9. The FEM mesh is then refined if needed until stress convergence at this particular point is reached. ε was set to $10^{-2}mm = 10\mu m$. It was indeed considered that experimentally ensuring the local geometry at this scale was already a great performance for adhesive bonding. It is worth noticing that the stresses computed at point A are related to both λ and $\underline{\underline{F}}$ defined in equation (1) of the analytic analysis.

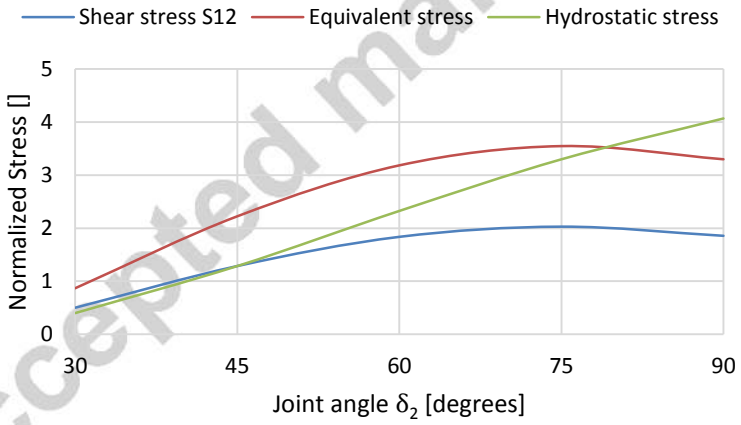

Figure 18: Evolution of the shear stress, the equivalent stress and the hydrostatic stress with the joint angle δ_2

Figure 18 shows that a larger joint angle reinforces significantly the stress level at this point A. In particular, the hydrostatic stress increases linearly with the joint angle whereas the shear and equivalent stress saturate. Therefore, one can expect early failures in the angles due to apparition of tensile stresses, which overcome the effect of the shear stresses during fatigue tests.

The evolution of the triaxiality ratio along the joint-substrate interface was also investigated and is illustrated on Figure 19

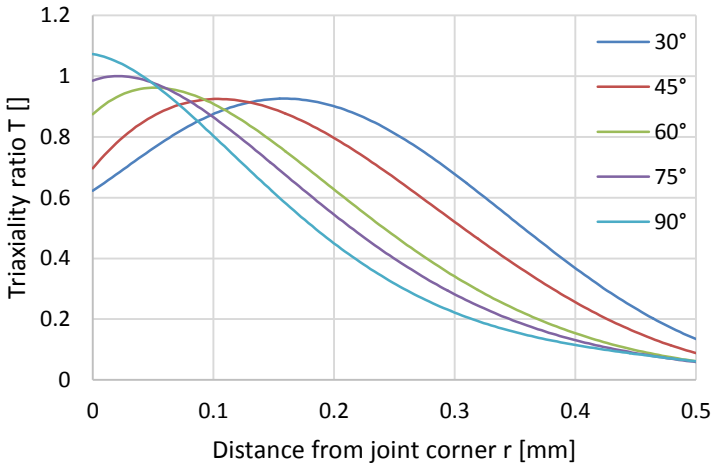

Figure 19: Triaxiality ratio evolution along joint-substrate interface

As expected, the triaxiality ratio at the corner of the joint increases when increasing the joint angle. It is interesting to notice that when the angle is sharpened, the triaxiality ratio reaches a maximum asymptotic value about $T = 0.92$, but this value is then reached inside the joint, more and more far away form the corner as the angle is reduced. As fatigue cracks are known to be sensitive to the surface defect of the samples, unloading the free surface of the joint at the expense of the inside can be a good point for its behavior in fatigue.

At last, it is clear here that the curves obtained in the two previous figures do not depend on the joint stiffness E_2 or G_2, as all boundary conditions are formulated in displacement and all studied mechanical quantities in these graphs (normalized stresses and triaxiality ratio) are dimensionless. Only the Poisson's ratio of the joint ν_2 matters.

6. Proposal of a hybrid setup

For fatigue purposes, it is of interest to have a flexible test setup with a small and simple substrate geometry. This will also facilitate delays and diminish production costs. That's why a design for a tensile test machine inspired from called the "modified TAST fixture" (see Figure 20) is now proposed. It takes advantage of the simplicity of a lap shear/TAST design and of the boundary conditions of the ARCAN that prevent the triaxiality ratio to become substantial.

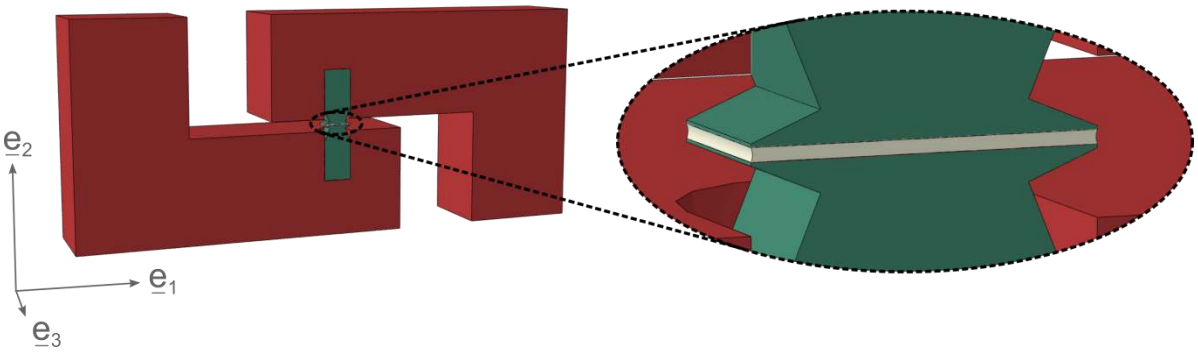

Figure 20: Sectional view of the geometry of the home-made "modified TAST fixture" method

The joint shape was set to a small square with side length about $5\ mm$ to reduce the shear stress heterogeneity. The substrates are made in aluminum to lower the material discontinuity between joint and substrate and because it is one of the most common metals but also one of the easiest to machine. A special machining was released to get substrate angles of $\delta_1 = 30°$ on both sides. The L-shaped parts are made of steel to minimize the bending phenomenon and prevent normal stresses.

This geometry was investigated numerically with ABAQUS®. A 3D model is used to take into account all potential thru-width effects. Given the symmetry of the configuration with respect to the plane $z = w/2$ (see the conventions exposed in the part 3), only a half of the configuration ($z \leq w/2$) will be modelled. The symmetry condition for the material surfaces on the plane $z = w/2$ simply reads $u_3 = 0$. The global rules for mesh refinement used in the previous computation are also applied here. The joint is meshed with hexahedral quadratic elements C3D20RH with reduced integration and hybrid formulation. For computational speed considerations, linear wedge elements C3D6 and tetrahedral elements C3D4 were used for the aluminum substrates and steel parts respectively. The material parameters for the joint and the substrates are the same as those used in paragraph 5.1:

$$\begin{cases} G_{joint} = 100\ MPa \\ \nu_{joint} = 0.49 \\ E_{aluminum} = 70\ GPa \\ \nu_{aluminum} = 0.33 \end{cases}$$

Concerning the steel parts, the following material constants are considered:

$$\begin{cases} E_{steel} = 210\ GPa \\ \nu_{steel} = 0.30 \end{cases}$$

The loading is imposed in terms of displacement as for the previous computations at the extremity of both steel parts:

- $\underline{u} = \underline{0}$ at the extremity of the left steel part
- $\underline{u} = d\underline{e_1}$ at the extremity of the right steel part

The joint thickness is here set to $h = 200\ \mu m$. The Figure 21 shows the deformed state of the proposed setup for the macroscopic imposed shear strain $\gamma_0 = d/h = 2$, with an isolated zoom on the joint. The normalized strain γ_{12}/γ_0 has been plotted.

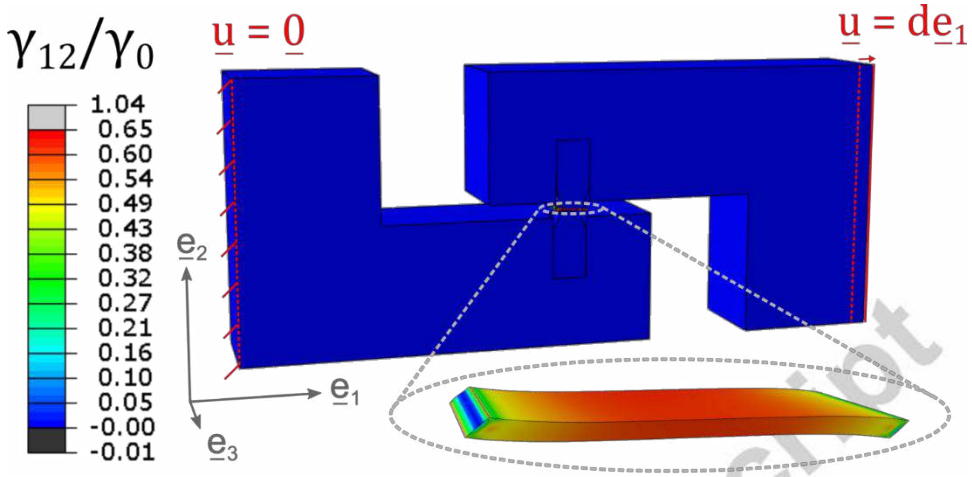

Figure 21: Deformed states for $\gamma_0 = d/h = 2$ with a zoom on the joint area for the proposed geometry

The Figure 22 presents the normalized shear stress τ_n and triaxiality ratio T distribution within the simulated half-joint ($z \leq w/2$), with a plot for $x \in [0\ ; L]$ in the midplane $y = h/2$, $z = w/2$.

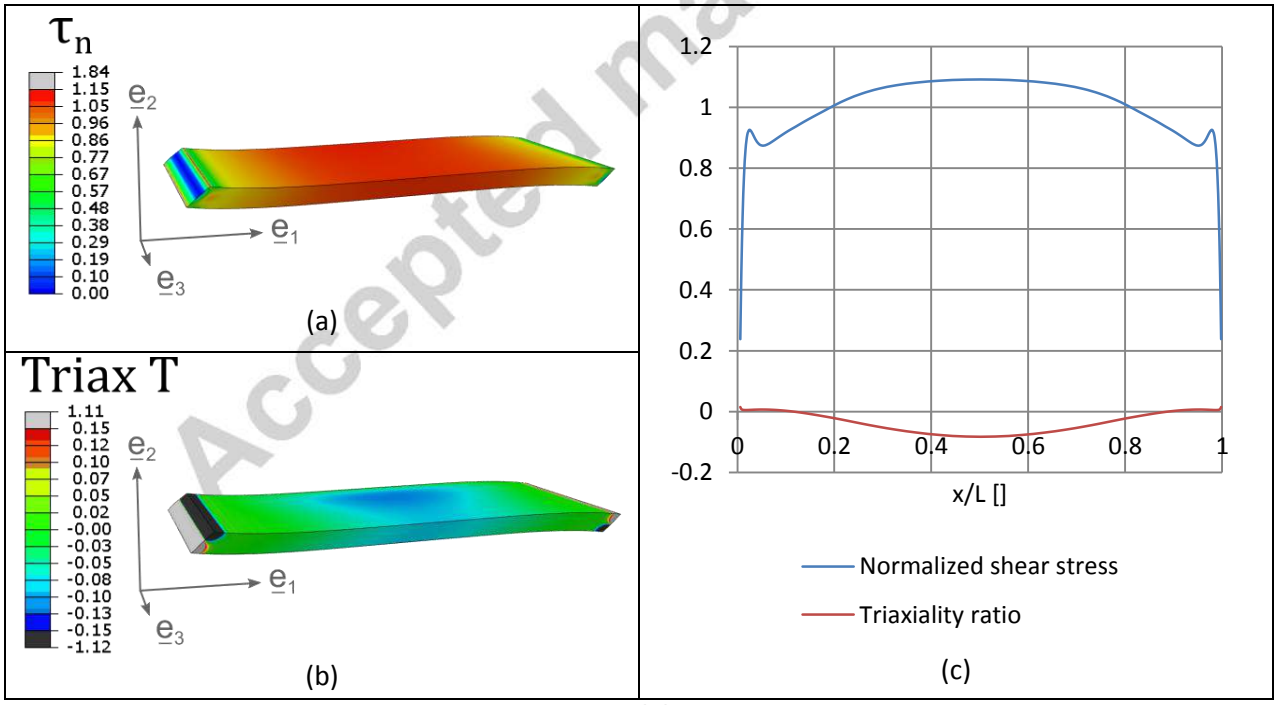

Figure 22: Mechanical fields in the half joint for loading $\gamma_0 = d/h = 2$: normalized shear stress τ_n distribution (a) ; triaxiality ratio T distribution (b) ; plot of τ_n and T within joint length L for $y = h/2$ and $z = w/2$

The Figure 22 (c) illustrates the shear stress non-uniformity because of the grooves on the substrates. These grooves induce a decrease of the stress in the joint end areas. Consequently, the highest shear stress is located at the center of the joint $x = L/2$ and the value reached is about

$$\sigma_{12}(L/2) = 1.1 \times \overline{\tau} = 1.1 \times F/S$$

However, the 1.1 coefficient noticed between the local stress and the average stress changes with the joint stiffness G_{joint}. As a matter of fact, this coefficient converges to 1 when the joint over substrate stiffness ratio $G_{joint}/E_{aluminum}$ goes to 0, and increases with $G_{joint}/E_{aluminum}$. This phenomenon prevents to consider the mean shear stress $\overline{\tau}$ as well as the mean shear strain $\overline{\gamma} = \delta/h$ defined in paragraph 5.1 to be representative of the joint solicitation during loading. To overcome this disadvantage, abacus were computed that give relevant mechanical quantities such as the secant joint modulus G_{joint}, the local maximum shear stress $\tau(L/2)$ and strain $\gamma(L/2)$ in function of the macroscopic setup response F/d for different joint thicknesses h. An example of these abacus for the joint stiffness G_{joint} is displayed on Figure 23:

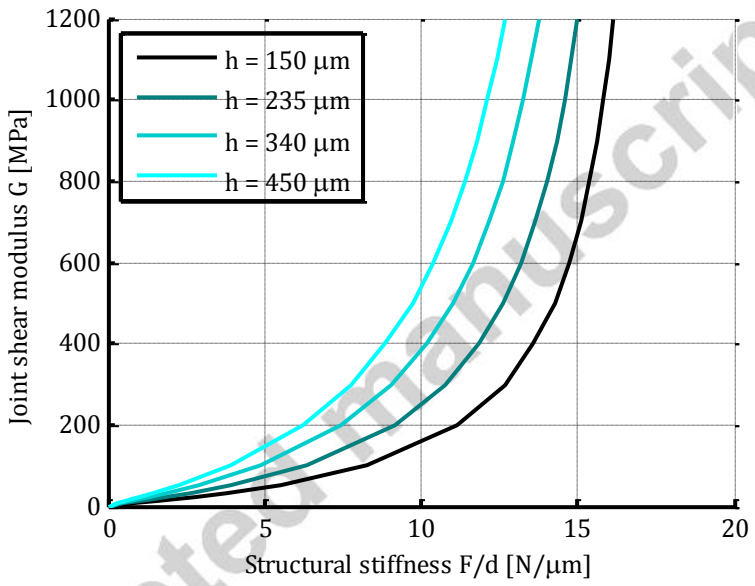

Figure 23: Abacus of the joint shear modulus G in function of the macroscopic stiffness F/d for four different joint thicknesses h

For an adhesive joint described by a strongly non-linear constitutive law, an additional numerical optimization procedure has to be implemented to get the law parameters from the fit of the macroscopic variables $F(d)$.

This setup was used to study the fatigue strength of two commercial Electrically Conductive Adhesives used in the framework of the electronic industry: a polyimide joint, and a silicone joint. The $5 \times 5\ mm^2$ area of the joint particularly fits to the electronic applications, whose adhesive joints are usually smaller than structural adhesive joints. These two adhesives are both filled with silver particles up to a volume fraction higher than 50% to be electrically conductive. However, their bulk behavior is extremely different, as the silicone matrix is in the rubbery state at room temperature whereas the polyimide matrix is in the glassy state at room temperature. It is therefore expected that the polyimide joint presents a much stiffer shear modulus at small strain than the silicone joint. In addition, the uncured polyimide paste contains a solvent, whose evaporation during curing causes the formation of numerous voids inside the polyimide joint. On the contrary, no solvent is present in the uncured silicone paste, such

that no void arises during curing of the silicone joint. This latter point is illustrated with X-Ray pictures in Figure 24: they confirm the presence of void in the polyimide joint after curing and the absence of void in the silicone joint after curing.

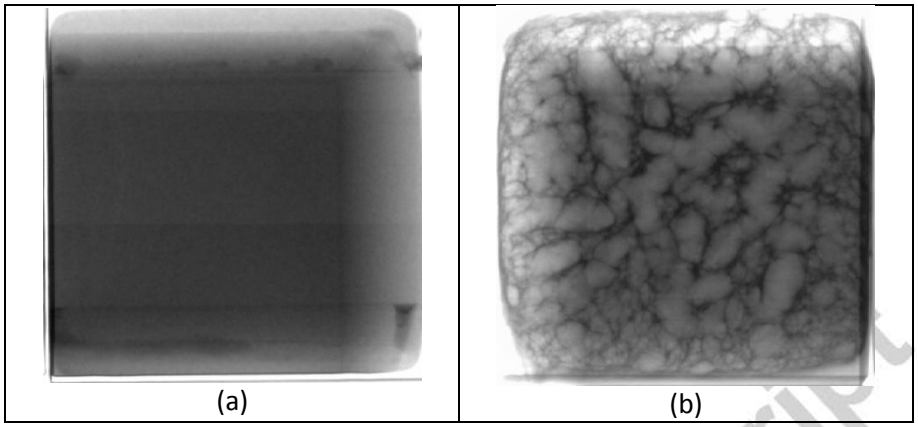

Figure 24: X-ray views of the cured silicone joint (a) and the polyimide joint (b). The side of the joint is $5\ mm$ long.

The substrates used were machined from an A2618 aluminum. To match with the electronic applications, these substrates were polished to reach the small roughness of electronic board pads used in electronic assemblies, which arithmetic roughness R_a generally lies below $1\ \mu m$. They were then plated in a 7 to $10\ \mu m$-thick electroless nickel-phosphorus layer and a $0.1\ \mu m$-thick electrolytic gold layer to reproduce the classical pad plating used in electronic assemblies. The whole test setup is mounted in a BOSE 3330 series II tensile machine with a $\pm\ 500N$ range load cell. The displacement $d_{crosshead}$ measured at the crosshead level is corrected by the machine compliance $S_{machine}$ experimentally determined to get the displacement d at the setup level:

$$d = d_{crosshead} - S_{machine} \times F$$

The Figure 25 shows a bonded sample, the test setup mounted in the tensile test machine, and the tooling used to assure the substrate alignment and the thickness control during sample curing. Joint thickness was set to $h = 250\ \mu m$, and controlled with optical microscopy after curing.

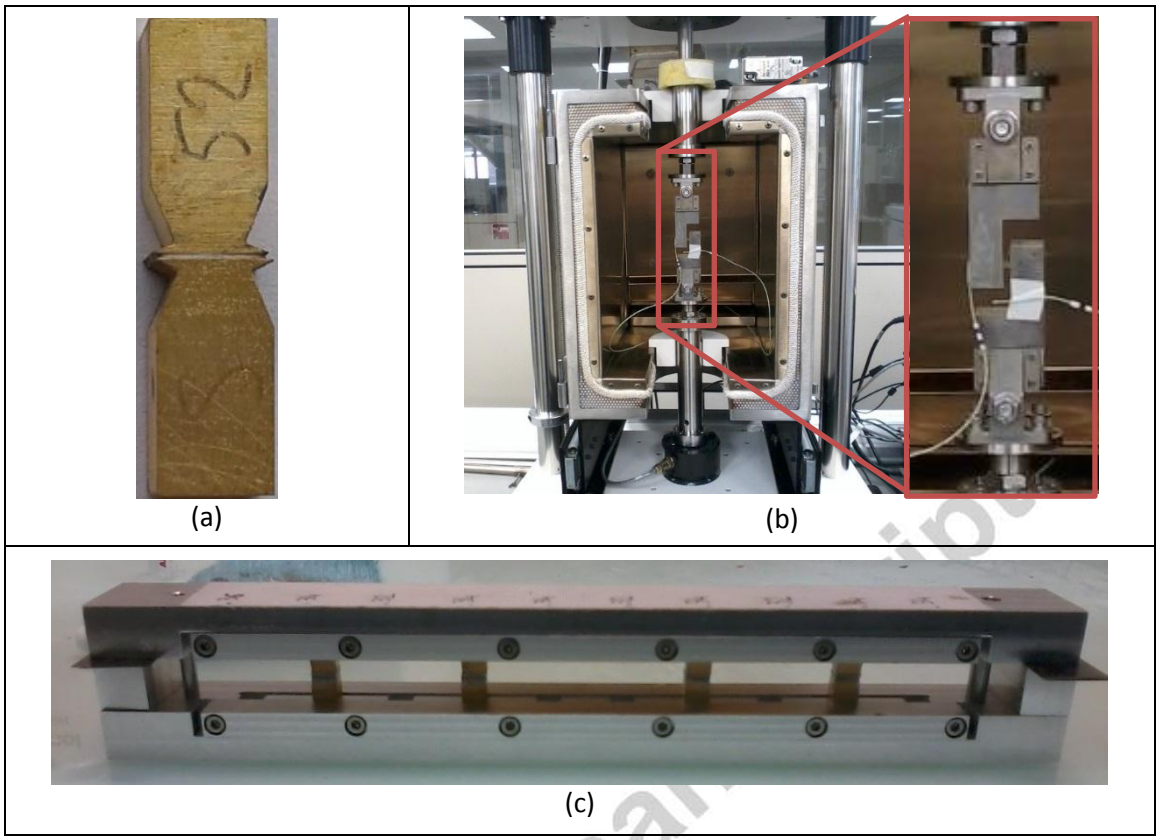

Figure 25: bonded sample (a) ; test setup mounted in the tensile machine (b) ; special tooling used to bond up to 10 samples simultaneously (c)

The fatigue results will be presented in a coming paper. Nonetheless, this paper presents as an illustration of the setup the monotonic shear response for each adhesive obtained with the hybrid geometry proposed. Both monotonic shear tests were conducted at macroscopic constant load rate $\dot{F}$. Once the yield stress of the joint is reached, the secant modulus τ/γ decreases. As a consequence, the shear strain rate increases because of the constant load rate control. This phenomenon is however also present with a constant crosshead velocity $\dot{d}_{crosshead}$, although less pronounced. The Figure 26 presents the monotonic shear behavior obtained of the silicone joint, and the Figure 27 shows the behavior of the polyimide joint.

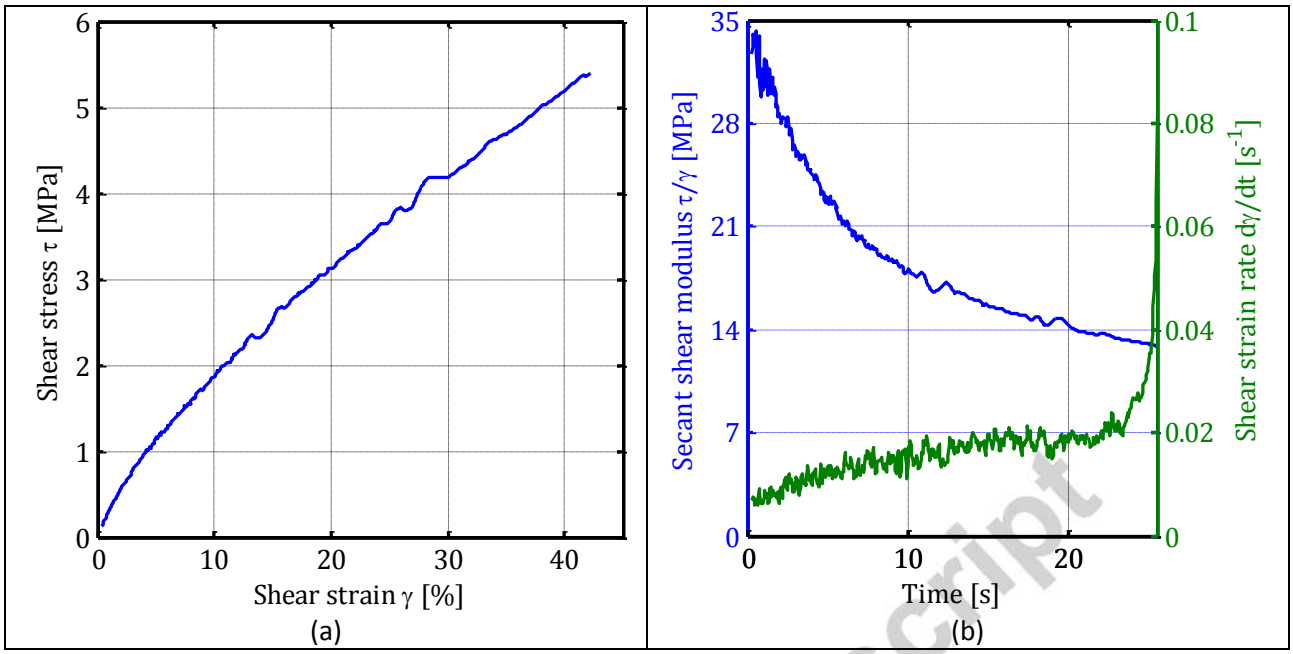

Figure 26: Results of a monotonic shear test on the silicone joint

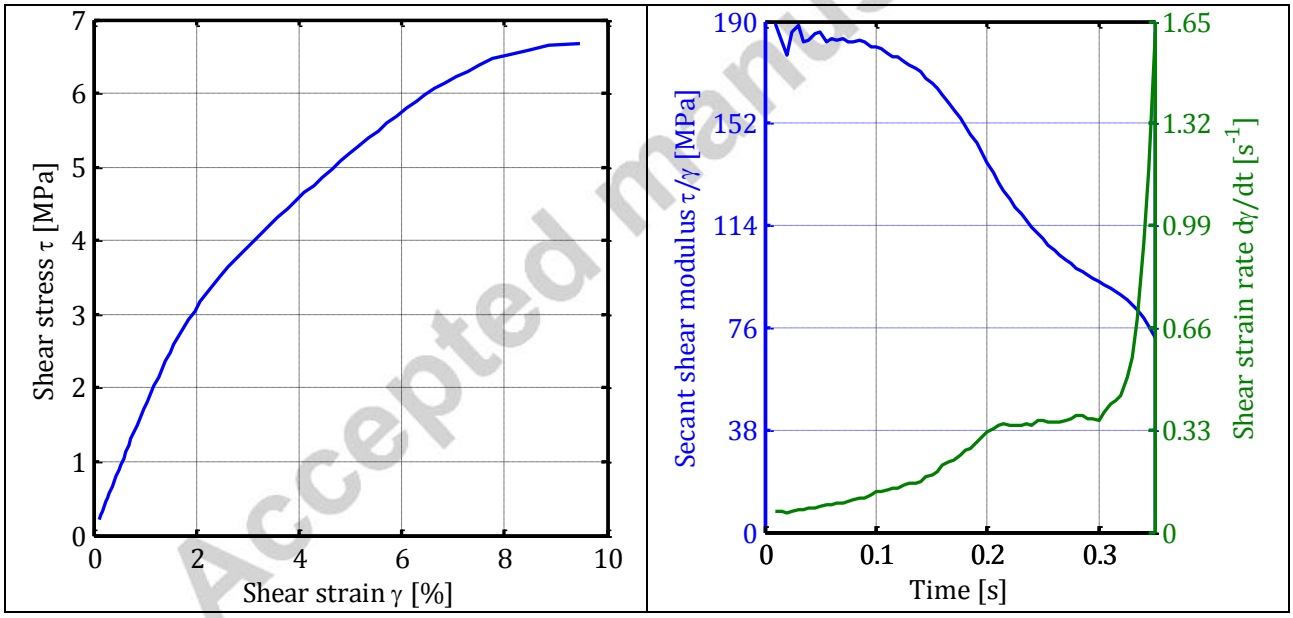

Figure 27: Results of a monotonic shear test on the polyimide joint

The experiments exhibit a shear modulus at small strain of 31 MPa and 184 MPa for silicone and polyimide respectively. The linear relation between shear stress τ and strain γ remains graphically valid up to a shear strain $\gamma = 1.5$ % for both joints. For larger strains, the stress-strain curve starts to bend and the shear strain starts to rise until failure. The shear modulus of the silicone joint is approximatively one order of magnitude higher than the stiffness of typical homogeneous silicone matrix, showing the reinforcement effect of the silver particles used for the electrical properties of the joint. However, the shear modulus of the polyimide joint is one order of magnitude lower than the stiffness of typical polyimide matrix. This phenomenon can be explained by the voids initiated in the polyimide joint during the curing process.

7. Conclusions

The analysis of the stress states of four standard joint shear testing setups has shown that:

- The homogeneity of the shear stress is highly deteriorated in case of substrate deformation during loading. Verifying that the substrate material is much stiffer than the tested joint is actually not sufficient, one has to take into account the structural stiffness of the whole assembly to ensure substrate rigidity compared to the adhesive joint.
- Normal stress concentrations (characterized by a triaxiality ratio reasonably far away from 0) can arise even for thick and stiff substrates (e.g. TAST) as soon as the macroscopic vertical movement of the substrates (due to bending for example) is not structurally prohibited by the setup design.

As a direct consequence of the two preceding remarks, the ARCAN setup is the most suitable method for a tensile testing machine whereas the napkin ring method is well adapted to a twisting machine. The numerical response of each test method compared to the non-linear constitutive law implemented (see Figure 17) clearly shows the dramatic consequences of neglecting these two points

Independently of the chosen test method, it has been proven that the local interfacial geometry of the joint conducts to a stress singularity at the joint corner, i.e. analytically infinite value s and practically higher values than damage limits. Moreover, it was shown that sharp angles for both joint and substrate will diminish the stress concentration. This can be obtained by a special machining of the substrates. Last but not least, as joint are generally polymer based, one should introduce the effects of curing process on the joint geometry, to ensure that the shapes of the joint after polymerization are in agreement with the criteria for the sharp angles. As a final remark, this kind of singularity unavoidably induces early cracks . Therefore, controlling the corner angle of the joint in relation with the stiffness ratios is decisive in the design of the joint test method.

All the preceding observations about the effect of different geometric and material parameters upon the stress state of the adhesive joint in a bonded assembly permits to design an optimal test setup of adhesive joints in shear loading taking into account not only the distribution of the shear stress but equally the distribution of the triaxiality ratio. The results will not be biased by the initiation of early cracks due to normal stresses and/or stress singularities.

Moreover, the conclusion enabled to construct an experimental setup for fatigue testing of Electrically Conductive Adhesives. The analysis of the setup showed proved that shear and triaxiality distributions stayed close to constant in spite of the small scale of the specimen. A complete fatigue analysis of the experiments is in preparation.

Appendix:

A. Influence of joint thickness

The influence of joint thickness has also been briefly investigated. To this end, the lap shear stress repartition is first compared for three different joint lengths L and thicknesses h, all material data being the same as presented in section 3 (in particular, the model is linear elastic):

- $L = 10\ mm$, $h = 1\ mm$ $(h/L = 0.1)$
- $L = 30\ mm$, $h = 1\ mm$ $(h/L = 0.033)$
- $L = 30\ mm$, $h = 3\ mm$ $(h/L = 0.1)$

Hence comparing configurations 1 and 3 will give how L/h-dependent the shear stress repartition at joint mid-plane is, whereas the comparison of configurations 2 and 3 will give the h dependence of the shear stress.

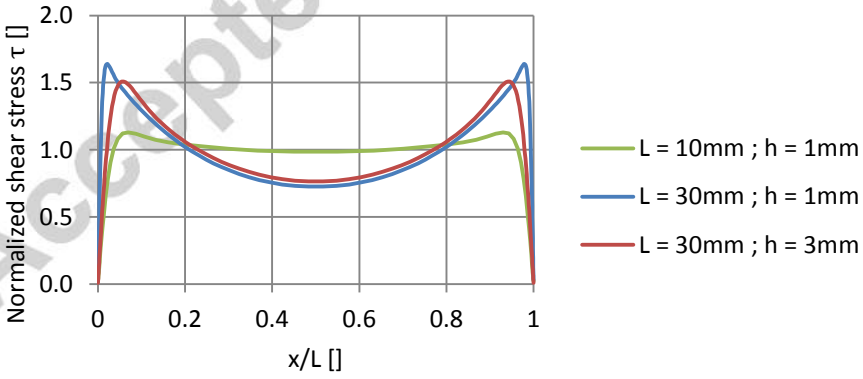

Figure 28: Shear stress repartition in lap shear joint for different $\mathrm{h/L}$ ratios

Curve 2 (blue) and 3 (red) on Figure 28 are much closer to each other than curve 1 (green) and 3 (red), indicating that the shear stress is rather thickness-independent than L/h-dependent.

Second, the influence of the thickness on the triaxiality ratio is also quickly explored, in the particular case of the lap shear geometry with $L = 30\ mm$. The thickness was varied from $1\ mm$ to $5\ mm$. The

triaxiality ratio repartition in the joint mid-plane for three different values of the thickness is plotted in Figure 29.

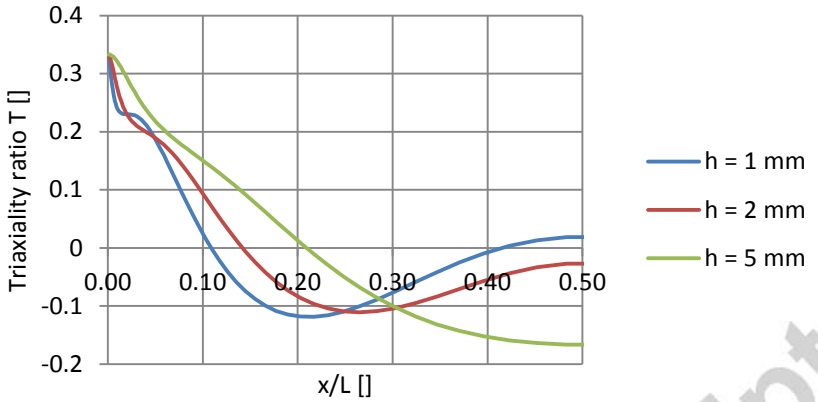

Figure 29 : Triaxiality ratio repartition in lap shear joint for different h values with $L = 30\ mm$

The Figure 29 shows by comparison with Figure 13 (b) that increasing the joint thickness h has the same consequence on the triaxiality ratio evolution than decreasing the joint length L. This remark implies that, contrary to the shear stress repartition, the triaxiality ratio repartition is h/L-dependent rather than h-independent.

B. Elastic analysis for viscoelastic materials

To justify the use of purely elastic numerical computations for usually viscoelastic materials, a relaxation test with the joint alone was simulated with a viscoelastic behavior. The FEM model is the same as the one used to assess the edge effects and illustrated in Figure 11, with $\delta_2 = 90°$. The constitutive law considered was the simplest Prony's series with only one exponential decay and a long-term elastic modulus: $G_2(t) = G_2\left(1 - \alpha \exp(-t/\tau)\right)$, with $\alpha = 0.5$ and $\tau = 1s$. Given the boundary conditions imposed in displacement, the problem in terms of normalized stress becomes actually independent of the shear modulus of the joint G_2. This constitutive law was chosen because of its simplicity and not according to any experimental results. The normalized simple shear stress $\tau_n(x, y = h/2)$ distribution within joint length is plotted on Figure 30 for time points approximately equally distributed on a logarithmic scale: $0.05\ s$, $1\ s$ and $10\ s$. These time points include the time relaxation constant of the constitutive law τ used, and go far shorter and longer. The stress distribution obtained at the first time point can therefore be considered as the instantaneous response, whereas the distribution obtained for the last time point is closed to the long-term response. The curve obtained with a purely elastic constitutive law (corresponding in fact with the asymptotic joint response) is then superimposed on the figure.

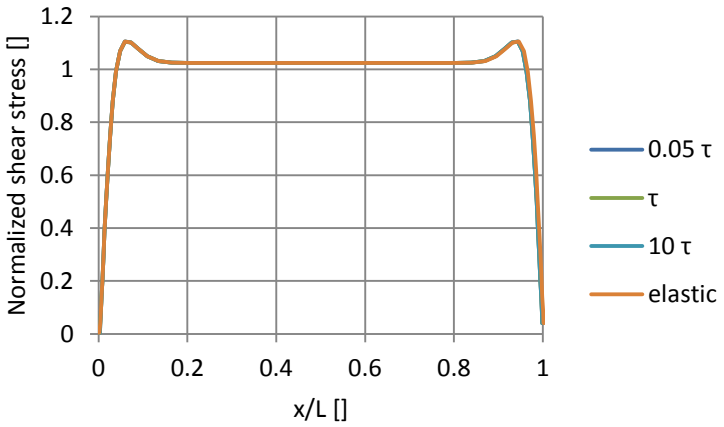

Figure 30: Shear stress repartition at different time points during a relaxation test and for an elastic response

All the plots look clearly similar: less than 2% deviation between the elastic distribution and any viscoelastic one for $0.06 \leq x/L \leq 0.94$ is noticed. Hence the hypothesis of separation of space and time variables: $\underline{\underline{\sigma}}_{visco}(x,y,t) = \underline{\underline{\sigma}}_{elastic}(x,y) \times f(t)$. The same verification was besides done for a cyclic solicitation by considering the stress repartition at different time points of the asymptotic cyclic response.

C. Expressions of hydrostatic and equivalent stresses σ_p and σ_{eq}

The exhaustive expressions for both σ_p and σ_{eq} in the case of a classical 3D-analysis read

$$\sigma_p = \frac{1}{3}\mathrm{tr}\left(\underline{\underline{\sigma}}\right) = \frac{1}{3}(\sigma_{11} + \sigma_{22} + \sigma_{33})$$

$$\sigma_{eq} = \sqrt{\frac{3}{2}\left(\underline{\underline{\sigma}} - \sigma_p\underline{\underline{I}}\right) : \left(\underline{\underline{\sigma}} - \sigma_p\underline{\underline{I}}\right)} = \frac{\sqrt{(\sigma_{11}-\sigma_{22})^2 + (\sigma_{22}-\sigma_{33})^2 + (\sigma_{33}-\sigma_{11})^2 + 6({\sigma_{12}}^2 + {\sigma_{23}}^2 + {\sigma_{13}}^2)}}{\sqrt{2}}$$

For a 2D-plane strain analysis, $\sigma_{13} = \sigma_{23} = 0$ and $\sigma_{33} = (1+\nu_i)(\sigma_{11}+\sigma_{22})$ with $i = 1$ for the substrate material and $i = 2$ for the adhesive material. Hence the expressions of σ_p and σ_{eq} simplify as following:

$${\sigma_p}^{2D} = \frac{1}{3}(1+\nu_i)(\sigma_{11}+\sigma_{22})$$

$${\sigma_{eq}}^{2D} = \frac{\sqrt{(\sigma_{11}-\sigma_{22})^2 + ((1-\nu_i)\sigma_{22}-\sigma_{11})^2 + ((1-\nu_i)\sigma_{11}-\sigma_{22})^2 + 6{\sigma_{12}}^2}}{\sqrt{2}}$$

D. Computation of the eigenvalue α for a bi-material wedge under 2D plane strain assumptions

This study has been conducted according to the method exposed in . A bi-material wedge is here considered, defined in terms of Lamé coefficients (λ, μ) or engineering constants (E, ν) by:

$(\lambda,\mu)=\begin{cases}(\lambda_1,\mu_1)\text{ for }0<\theta<\phi_1\\(\lambda_2,\mu_2)\text{ for }\phi_1<\theta<\phi_1+\phi_2\end{cases}$	$(E,\nu)=\begin{cases}(E_1,\nu_1)\text{ for }0<\theta<\phi_1\\(E_2,\nu_2)\text{ for }\phi_1<\theta<\phi_1+\phi_2\end{cases}$

(D.1)

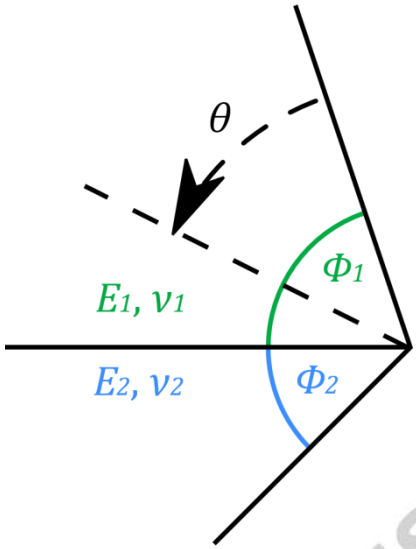

Figure 31: Bi-material wedge geometrical configuration

The displacement vector is taken of the form $\underline{u}(r,\theta)=r^{\alpha}\cdot\underline{U}(\theta)=r^{\alpha}\cdot\begin{pmatrix}U_r(\theta)\\U_\theta(\theta)\end{pmatrix}$ in polar coordinates.

Considering a test function of the form $\underline{v}(r,\theta)=f(r)\cdot\underline{V}(\theta)=f(r)\cdot\begin{pmatrix}V_r(\theta)\\V_\theta(\theta)\end{pmatrix}$, the problem is actually the balance of the forces in variational form: find the eigenvalue α such that for all $\underline{v}$,

$$\int_{r=0}^{\infty}\int_{\theta=0}^{\phi_1+\phi_2}\left(\underline{\underline{\varepsilon}}\left(\underline{u}(r,\theta)\right):\underline{\underline{\underline{\underline{C}}}}(\theta):\underline{\underline{\varepsilon}}\left(\underline{v}(r,\theta)\right)\right)r\mathrm{d}r\mathrm{d}\theta=0$$

This burns down to the eigenvalue problem only when the displacement field $\underline{u}$ has the given form, and leads to a generalization of the Williams wedge problem mentioned in subsection 5.2.

Taking into account that $\int_0^{\infty}r^{\alpha}f'(r)\mathrm{d}r=-\alpha\int_0^{\infty}r^{\alpha-1}f(r)\mathrm{d}r$ (the boundary term vanishes at infinity when $f\in\mathcal{D}(0,+\infty)$), the previous relation then becomes

$$\left(\int_{r=0}^{\infty}r^{\alpha-1}f(r)\mathrm{d}r\right)\left(-\alpha^2b_2\left(\underline{U},\underline{V}\right)+\alpha b_1\left(\underline{U},\underline{V}\right)+b_0\left(\underline{U},\underline{V}\right)\right)=0$$

with the following expressions for the b_k:

$$\begin{cases} b_2(\underline{U},\underline{V}) = \int_{\theta=0}^{\phi_1+\phi_2} [(\lambda+2\mu)U_rV_r + \mu U_\theta V_\theta]\,\mathrm{d}\theta \\ b_1(\underline{U},\underline{V}) = \int_{\theta=0}^{\phi_1+\phi_2} [\mu(-U_r{}'V_\theta + U_\theta V_r{}') + \lambda(-U_\theta{}'V_r + U_rV_\theta{}')]\,\mathrm{d}\theta \\ b_0(\underline{U},\underline{V}) = \int_{\theta=0}^{\phi_1+\phi_2} [\mu(U_\theta V_\theta - U_r{}'V_\theta - U_\theta V_\theta{}' + U_r{}'V_r{}') + (\lambda+2\mu)(U_rV_r + U_\theta{}'V_r + U_rV_\theta{}' + U_\theta{}'V_\theta{}')]\,\mathrm{d}\theta \end{cases}$$

Here, λ and μ as well as $\underline{U}$ and $\underline{V}$ are function of θ (see equation (D.1)).

The numerical resolution is based on a discretization of the space $\mathcal{H}^1(0,\phi_1+\phi_2)$: the segment $[0\ ;\ \phi_1+\phi_2]$ is divided into $N-1$ sub-segments (providing N nodes). The shape functions $w_i$are piecewise-linear and vanishes at each node except node i where it equals 1. The 2D basis function is then built in polar coordinates as $\underline{w}_{2i-1} = \begin{pmatrix} w_i \\ 0 \end{pmatrix}$ and $\underline{w}_{2i} = \begin{pmatrix} 0 \\ w_i \end{pmatrix}$.

The next step is to compute the B_k matrix:

$$\forall i,j \in [0\ ;2N]\ , B_k(i,j) = b_k(\underline{w}_i,\underline{w}_j)\ ,\ \ (k=2,1,0)$$

And finally find the smallest eigenvalue a such that $\mathrm{Det}(A(\alpha)) = 0$ with $A(\alpha) = -\alpha^2 B_2 + \alpha B_1 + B_0$.

The Matlab code is available upon request. This method can also be generalized to anisotropic materials and therefore applied to composite material. In this case, one would take care of the computation of the energy integral in the variational form as the expression of the stiffness tensor $\underline{\underline{\underline{\underline{C}}}}$ can be much more complex and maybe more simple to manipulate in a Cartesian basis. The reader is referred to for further information on the method.

E. Constitutive law parameters used for the simulation of the behavior of the epoxy Ciba AV119

As explained in the article, the constitutive is linear elastic and plastic with isotropic non-linear hardening.

Elastic part: $G = 1075\ MPa, \nu = 0.49$

Plastic part: $\sigma_0 = 15.336\ MPa$

Table E.7: Values of the piecewise-linear hardening parameter

q []	$R(q)$ $[MPa]$
0	0
0.000113	10.224
0.00036	15.637
0.001039	25.860
0.002078	33.829

0.00305	39.091
0.004362	44.354
0.006593	50.669
0.00911	55.329
0.011121	58.336
0.013025	60.592
0.015589	62.546
0.019059	64.501
0.02378	65.704
0.028395	66.155
0.090205	66.155

References

[1] R. D. Adams, J. Comyn and W. C. Wake, Structural adhesive joints in engineering, Springer Science & Business Media, 1997.

[2] E. Jarry and R. A. Shenoi, "Performance of butt strap joints for marine applications," *International journal of adhesion and adhesives,* vol. 26, no. 3, pp. 162-176, 2006.

[3] M. J. Cowling, "A review of adhesive bonding for offshore structures," Health and Safety Executive, 1997.

[4] L. Li and J. E. Morris, "Reliability and failure mechanism of isotropically conductive adhesive joints," in *Electronic components and technology conference*, 1995.

[5] O. Rusannen and J. Lenkkeri, "Thermal stress induced failures in adhesive flip chip joints," *International journal of microcircuits and electronic packaging,* vol. 22, no. 4, pp. 363-369, 1999.

[6] R. Dudek, H. Berek, T. Fritsch and B. Michel, "Reliability investigations on conductive adhesive joints with emphasis on the mechanics of the conduction mechanism," *IEEE Transactions on components and packaging technologies,* vol. 23, no. 3, pp. 462-469, 2000.

[7] R. D. Adams, J. Coppendale and N. A. Peppiatt, "Stress analysis of axisymmetric butt joints loaded in torsion and tension," *The Journal of Strain Analysis for Engineering Design,* vol. 13, no. 1, pp. 1-10, 1978.

[8] Q. D. Yang, M. D. Thouless and S. M. Ward, "Elastic-plastic mode-II fracture of adhesive joints," *International Journal of Solids and Structures,* vol. 38, no. 18, pp. 3251-3262, 2001.

[9] J.-Y. Cognard, R. Creac'Hcadec and J. Maurice, "Numerical analysis of the stress distribution in single-lap shear tests under elastic assumption - Application to the optimisation of the mechanical bahevior," *International journal of adhesion and adhesives,* pp. 715-724, 2011.

[10] S. K. Parida and A. K. Pradan, "Influence of curvature geometry of laminated FRP composite panels on delamination damage in adhesively bonded lap shear joints," *International Journal of Adhesion and Adhesives,* vol. 54, pp. 57-66, 2014.

[11] Y. Boutar, S. Naimi, S. Mezlini and M. Ali, "Effect of surface treatment on the shear strength of aluminium adhesive single-lap joints for automotive applications," *International Journal of Adhesion and Adhesives,* vol. 67, pp. 38-43, 2016.

[12] U. T. Carvalho and R. D. S. G. Campilho, "Validation of pure tensile and shear cohesive laws obtained by the direct method with single-lap joints," *International Journal of Adhesion and Adhesives,* vol. 77, pp. 41-50, 2017.

[13] J.-Y. Cognard, R. Creac'Hcadec, L. Sohier and P. Davies, "Analysis of the non-linear bahevior of adhesives in bonded assemblies - Comparison of TAST and ARCAN tests," *International journal of adhesion and adhesives,* vol. 28, no. 8, pp. 393-404, 2008.

[14] A. B. de Morais, A. B. Pereira, J. P. Teixeira and N. C. Cavaleiro, "Strength of epoxy adhesive-bonded stainless-steel joints," *International Journal of Adhesion and Adhesives,* vol. 27, no. 8, pp. 679-686, 2007.

[15] J.-Y. Cognard, P. Davies, B. Gineste and L. Sohier, "Development of an improved adhesive test method for composite assembly design," *Composites science and technology,* pp. 359-368, 2005.

[16] R. R. de Sousa Jr, J. R. Gouveia, N. M. Ito and D. J. dos Santos, "Failure prediction of hybrid composite using Arcan's device and Drucker-Prager model," vol. 58, pp. 256-261, 2017.

[17] R. Créac'Hcadec, L. Sohier, C. Cellard and B. Gineste, "A stress concentration-free bonded arcan tensile compression shear test specimen for the evaluation of adhesive mechanical response," *International Journal of Adhesion and Adhesives,* vol. 61, pp. 81-92, 2015.

[18] B. Vales, S. Marguet, R. Créac'Hcadec, L. Sohier, J.-F. Ferrero and P. Navarro, "Experimental and numerical study of the Tensile/Compression-Shear Arcan test under dynamic loading," *International Journal of Adhesion and Adhesives,* vol. 78, pp. 135-147, 2017.

[19] X. Buch, Degradation thermique et fluage d'un adhesif structural epoxyde, 2000.

[20] N. Arnaud, R. Créac'Hcadec and J.-Y. Cognard, "A tension/compression--torsion test suited to analyze the mechanical behaviour of adhesives under non-proportional loadings," *International Journal of Adhesion and Adhesives,* pp. 3-14, 2014.

[21] A. M. Pinto, A. G. Magalhaes, R. D. Campilho, L. F. Silva, J. A. Chousal and A. P. Baptista, "Shear modulus and strength of an acrylic adhesive by the notched plate shear method (ARCAN) and the tick adherent shear test (TAST)," *Materials Science Forum;,* Vols. 636-637, 2010.

[22] J. Deng, "Test methods for mechanical properties of structural adhesives," *Advanced Material Research,* vol. 97, pp. 814-817, 2010.

[23] J.-Y. Cognard, M. Bourgeois, R. Créac'Hcadec and L. Sohier, "Comparative study of the results of various experimental tests used for the analysis of the mechanical behaviour of an adhesive in a bonded joint," *Journal of Adhesion Science and Technology,* vol. 25, pp. 2857-2879, 2011.

[24] M. M. Abdel Wahab, I. Hilmy, I. A. Ashcroft and A. D. Crocombe, "Evaluation of fatigue damage in adhesive bonding: part 2: single lap joint," *Journal of Adhesion Science and Technology,* vol. 24, no. 2, pp. 325-345, 2010.

[25] A. Constantinescu and A. M. Korsunsky, Elasticity with Mathematica, Cambridge University Press, 2007.

[26] R. W. Soutas-Little, Elasticity, Courier corporation, 1999.

[27] M. L. Williams, "Stress singularities resulting from various boundary conditions in angular corners of plates in extension," *Journal of applied mechanics,* vol. 19, no. 4, pp. 526-528, 1952.

[28] D. Leguillon and E. Sanchez-Palencia, Computation of singular slutions in elleptic problems and elasticity, John Wiley & Sons, 1987.

[29] G. D. Dean, B. C. Duncan, R. D. Adams, R. Thomas and L. Vaughn, "Comparison of bulk and joint specimen tests for determining the shear properties of adhesives," 1996.

[30] J. C. Simo and T. J. Hughes, Computational inelasticity, vol. 7, 2006.

[31] B. C. Duncan and G. D. Dean, "Test Methods for Determining Shear Property Data for Adhesives Suitable for Design-Part 1: Notched-Beam (Iosipescu) and Notched-Plate (Arcan) Methods for Bulk and Joint Test Specimens," 1996.

[32] J.-Y. Cognard, R. Creac'Hcadec, L. Sohier and D. Leguillon, "Influence of adhesive thickness on the behavior of bonded assemblies under shear loadings using a modifiest TAST fixture," *International journal of adhesion and adhesives,* pp. 257-266, 2010.

[33] J.-P. Jeandrau, C. Peyrac, F. Lefebvre, J. Renard, V. Gantchenko, B. Patamaprohm and C. Guinault, "Fatigue Behaviour of Adhesive Joints," *Procedia Engineering,* vol. 133, pp. 508-517, 2015.

[34] N. G. Berry and J. R. Almeida, "The influence of circular centered defects on the performance of carbon-epoxy single lap joints," *Polymer Testing,* vol. 21, no. 4, pp. 373-379, 2002.

[35] H. K. Kim, J. G. Kim, J. D. Cho and J. W. Hong, "Optimization and characterization of UV-curable adhesives for optical communications by response surface methodology," *Polymer Testing,* vol. 22, no. 8, pp. 899-906, 2003.

[36] D. C. Moreira and L. C. Nunes, "Comparison of simple and pure shear for an incompressible isotropic hyperelastic material under large deformation," *Polymer Testing,* vol. 32, no. 2, pp. 240-248, 2013.

[37] F. Khan, J.-H. Koo, D. Monk and E. Eisbrenner, "Characterization of shear deformation and strain recovery behavior in shape memory polymers," *Polymer testing,* vol. 27, no. 4, pp. 498-503, 2008.

[38] F. Y. Boey, "Humidity and autoclave pressure effect on the interfacial shear strength of a microwave cured epoxy-glass fibre composite," *Polymer Testing,* vol. 14, no. 5, pp. 471-477, 1995.

[39] T. Sawa, Y. Nakano and K. Temma, "A stress analysis of butt adhesive joints under torsional loads," *The Journal of Adhesion,* vol. 24, no. 2-4, pp. 245-258, 1987.